B.1.1.7 and B.1.351 SARS-CoV-2 variants display enhanced Spike-mediated fusion

Maaran Michael Rajah[1,2], Mathieu Hubert[1,3,#], Elodie Bishop[1,4,#], Nell Saunders[1,#], Remy Robinot[1], Ludivine Grzelak[1,2], Delphine Planas[1,3], Marija Zivaljic[5,6], Cyril Planchais[7], Florence Guivel-Benhassine[1], Françoise Porrot[1], Hugo Mouquet[7], Lisa Chakrabarti[1] , Julian Buchrieser[1*] Olivier Schwartz[1,2*].

[1]Virus & Immunity Unit, Department of Virology, Institut Pasteur; CNRS UMR 3569, Paris, France

[2]Université de Paris, Sorbonne Paris Cité, Paris, France

[3]Vaccine Research Institute, Creteil, France

[4] Sorbonne Université, Paris F-75005, France[5]Integrative Neurobiology of Cholinergic Systems, Department of Neuroscience, Institut Pasteur; CNRS UMR 3571, Paris, France

[6]Sorbonne Université, ED3C "Brain, cognition, behavior", Paris, France

[7]Laboratory of Humoral Immunology, Department of Immunology, Institut Pasteur, INSERM U1222, Paris, France

[#] Second co-authors

*Last co-authors

Corresponding authors: julian.buchrieser@pasteur.fr; olivier.schwartz@pasteur.fr

Abstract

SARS-CoV-2 B.1.1.7 (variant Alpha) and B.1.351 (variant Beta) have supplanted pre-existing strains in many countries. Severe COVID-19 is characterized by lung abnormalities, including the presence of syncytial pneumocytes. Syncytia form when infected cells fuse with adjacent cells. The fitness, cytopathic effects and type-I interferon (IFN) sensitivity of the variants remain poorly characterized. Here, we assessed B.1.1.7 and B.1.351 spread and fusion in cell cultures. B.1.1.7 and B.1.351 replicated similarly to D614G reference strain in Vero, Caco-2, Calu-3 and primary airway cells and were similarly sensitive to IFN. The variants formed larger and more numerous syncytia. Variant Spikes, in the absence of any other viral proteins, resulted in faster fusion relative to D614G. B.1.1.7 and B.1.351 fusion was similarly inhibited by interferon induced transmembrane proteins (IFITMs). Individual mutations present in the variant Spikes modified fusogenicity, binding to ACE2 and recognition by monoclonal antibodies. Also, B.1.1.7 and B.1.351 variants remain sensitive to innate immunity components. The mutations present in the two variants globally enhance viral fusogenicity and allow for antibody evasion.

Introduction

SARS-CoV-2 was initially discovered during an outbreak in Wuhan, China, before it became pandemic (Huang *et al*, 2020). The ancestral Wuhan strain has since been supplanted by variants harboring a variety of adaptive mutations throughout the viral genome. One of the earliest identified variant displayed the D614G mutation in the Spike (S) protein, which increased viral infectivity without significantly altering antibody neutralization (Yurkovetskiy *et al*, 2020). Several other variants have emerged and become globally dominant, including B.1.1.7 (or variant alpha) first identified in the United Kingdom, B.1.351 (variant beta) identified in South Africa, P.1 (variant gamma) and P.2 identified in Brazil, and the B.1.617 lineage (including B.1.617.2 or variant delta) identified in India (Buss *et al*, 2021; Frampton *et al*, 2021; Planas *et al*, 2021b; Sabino *et al*, 2021; Tegally *et al*, 2020; Yadav *et al*, 2021). Some of these variants are more transmissible at the population level but their impact on disease severity is debated (Davies *et al*, 2021; Kemp *et al*, 2021; Korber *et al*, 2020). One characteristic of the variants is their ability to evade part of the neutralizing antibody response directed towards the S protein (Liu *et al*, 2021c; Planas *et al*, 2021a; Rees-Spear *et al*, 2021; Starr *et al*, 2021; Weisblum *et al*, 2020). This protein is important to the early stages of the viral life cycle. Virus-cell fusion occurs through the interaction of trimeric S with the ACE2 receptor and its subsequent cleavage and priming by TMPRSS2 and other cellular proteases (Hoffmann *et al*, 2020b). The conformational change induced by cleavage at the S1-S2 and S2' sites, allows for S to extend into the target membrane and trigger fusion (Dimitrov, 2004; Hoffmann *et al*, 2020a). Mutations in S are of

particular concern as they can modify antibody recognition, affinity to ACE2, proteolytic processing and incorporation into virions. It is therefore important to characterize how the mutations of the variants impact replicative fitness and cytopathic effects.

Clinically, SARS-CoV-2 infections range from febrile respiratory disorders to severe lung injury characterized by vascular thrombosis and alveolar damage (Bussani *et al*, 2020). The deterioration of respiratory tissue is likely a result of both virus-induced cytopathicity and indirect immune-mediated damage (Buchrieser *et al*, 2020; Zhang *et al*, 2020; Zhou *et al*, 2020; Zhu *et al*, 2020). A peculiar dysmorphic cellular feature of SARS-CoV-2 infection is the presence of large infected multinucleated syncytia, predominately comprised of pneumocytes (Braga *et al*, 2021; Bussani *et al.*, 2020; Sanders *et al*, 2021). Other coronaviruses including SARS-CoV-1, MERS-CoV, and HKU1 also induce fusion in infected patient tissue and primary cell culture systems (Chan *et al*, 2013; Dominguez *et al*, 2013; Franks *et al*, 2003; Qian *et al*, 2013). Mechanistically, syncytia formation is analogous to virus-cell fusion. The interaction of S present on the plasma membrane of infected cells with receptors and priming proteases on adjacent cells results in cell-cell fusion (Buchrieser *et al.*, 2020). Syncytial cells may compound SARS-CoV-2 induced cytopathicity, play a role in viral persistence and dissemination and could potentially be a pathological substrate for respiratory tissue damage (Braga *et al.*, 2021; Buchrieser *et al.*, 2020; Sanders *et al.*, 2021). There is a general paucity of information regarding how the mutations associated with the variant S proteins contribute to cellular pathology.

The interferon response to SARS-CoV-2 is one of the key factors down-modulating viral entry and replication, and deficiencies in the interferon response are associated with more severe COVID-19 (Arunachalam *et al*, 2020; Bastard *et al*, 2021; Bastard *et al*, 2020; Hadjadj *et al*, 2020; van der Made *et al*, 2020). SARS-CoV-2 induced syncytia formation by the Wuhan strain is restricted by innate immunity through the action of interferon induced transmembrane proteins (IFITMs) (Buchrieser *et al.*, 2020). IFITM1, 2 and 3 are restriction factors which display antiviral activity against a variety of enveloped viruses including SARS-CoV-2; likely by increasing membrane rigidity and hindering virus-cell fusion (Shi *et al*, 2021). Their effectiveness at restricting cell-cell fusion of novel variants has yet to be assessed.

Here we compared the replication, IFN sensitivity and syncytia forming potential of D614G, B.1.1.7, B.1.351 viruses in human cell lines and primary airway cells. We further characterize the fusogenicity of variant S proteins and the individual contribution of each of the component mutations in syncytia formation, ACE2 binding and evasion from a panel of antibodies.

Results

Comparative Replication Kinetics of SARS-CoV-2 Variants

We compared the replication kinetics of SARS-CoV-2 variants in relevant cell cultures. We first infected Caco-2, Calu-3 and Vero cells with the B.1.1.7, B.1.35, and D614G variants and generated multistep growth curves **(Fig. 1)**. Cell were infected at an equivalent, non-saturating

98 MOI, initially titrated in Vero cells **(Fig. EV1A)**. Viral replication was assessed at 24, 48, and 72
99 hours by flow cytometry upon staining with the pan-SARS-CoV-2 anti-S mAb102 human
100 monoclonal antibody (Planas *et al.*, 2021a) and then gating for S+ cells **(Fig. EV1B)**. Globally, the
101 variants replicated similarly **(Fig. 1)**. This similar replication was observed at different MOIs **(Fig.**
102 **EV1A)**. There were subtle differences at 24h post-infection, depending on the cell line and the
103 variant. For instance, B.1.351 replicated slightly more than D614G in Caco-2 cells whereas
104 B.1.1.7 replicated slight less than D614G in Vero cells **(Fig. 1A, C)**. Viral release at each time
105 point was also assessed by extracting RNA from the supernatant and performing RT-qPCR for
106 the SARS-CoV-2 N protein. Viral release was again roughly similar with the different variants,
107 especially at early time points. B.1.1.7 produced moderately more virus than D614G in all cell
108 lines at later time points **(Fig. 1A-C).** B.1.351 produced more virus than D614G in Caco-2 but
109 less in Calu-3 cells at later time points **(Fig. 1A, B)**.

110 As variants did not show any major difference in replication under basal conditions, we
111 next investigated if they were differently sensitive to the interferon response. To this aim, we
112 treated Vero Cells with different doses of IFN-β1 and infected them with the different variants.
113 IFN-β1 was equally effective at reducing viral replication of D614G, B.1.1.7, and B.1.351 variants
114 **(Fig. EV1C)**.

115 We then used the MucilAirB™ model, which consists of primary human airway epithelial
116 cells (HAEC) grown over a porous membrane and differentiated at the air-liquid interface for
117 over 4 weeks. This relevant model is susceptible to SARS-CoV-2 infection (Pizzorno *et al*, 2020;
118 Robinot *et al*, 2020; Touret *et al*, 2021). The cells were infected with each of the SARS-CoV-2

variants at a similar low viral inoculum (10^4 TCID50). Viral RNA and infectious virus release were monitored over 96h by RT-qPCR and TCID50. B.1.1.7 and B.1.351 variants produced slightly more extracellular viral RNA than D614G at later time points but not significantly higher levels of infectious particles **(Fig. 1D)**.

Taken together our data show that B.1.1.7 and B.1.351 variants replicate similarly to the ancestral D614G strain in a panel of human cell lines and in primary cells, with some slight differences. The variants are also similarly sensitive to IFN-β1 treatment.

Syncytia formation in cells infected with SARS-CoV-2 variants.

We next assessed the potential of SARS-CoV-2 variants to induce syncytia. In order to visualize cell-cell fusion, we employed our previously described S-Fuse assay, using U2OS-ACE2 GFP-split cells (Buchrieser *et al.*, 2020). In the GFP-split complementation system, two cell lines containing half of the reporter protein are co-cultured, producing a GFP signal only upon fusion **(Fig. 2A).** Upon infection of S-Fuse cells, we noticed that the B.1.1.7 and B.1.351 variants formed larger and more numerous infected syncytia than either D614G or the ancestral Wuhan strain **(Fig. EV2A).** We then characterized quantitatively the differences in fusogenicity by calculating the total syncytia (GFP) area and then normalizing it to nuclei number (Hoechst) **(Fig. EV2B)**. Relative to D614G, B.1.1.7 and B.1.351 variants produced significantly more syncytia, approximately 4.5 and 3-fold respectively, after 20h of infection with the same MOI **(Fig. 2B and EV3A)**. In order to characterize syncytia formation in a cell line expressing

endogenous ACE2, we generated Vero cells carrying the GFP-split system. After 48h of infection with the same MOI, we again found that B.1.1.7 and B.1.351 variants produced significantly more syncytia than D614G **(Fig. 2C and EV3B)** despite similar infection levels **(Fig. 1C)**. Of note, D614G produced similar levels of syncytia as the Wuhan strain in both Vero and S-Fuse cells (**Fig. 2 and EV3A-B**). Preincubation of S-Fuse cell with IFN-β1 abrogated infection and syncytia formation to the same extent with the different variants (**Fig. EV3C**).

Therefore, B.1.1.7 and B.1.351 variants appear more fusogenic than D614G in S-Fuse and Vero cells.

Syncytia formation in cells expressing variant Spikes.

Since syncytia formation is a consequence of the S protein expressed on the surface of an infected cell interacting with ACE2 receptors on neighboring cell, we sought to compare the fusogenic potential of the individual variant S proteins. We introduced the D614G mutation into the Wuhan protein and designed plasmids to express B.1.1.7 and B.1.351 S proteins. We transfected the respective plasmids into Vero GFP-split cells and quantified syncytia formation 18h later **(Fig. 3A)**. B.1.1.7 and B.1.351 S proteins were 2 and 1.7-fold more fusogenic than D614G S, respectively **(Fig. 3B)**. The Wuhan S was slightly less fusogenic that the D614G S **(Fig. 3B)**. We then verified that the variation in S mediated fusion was not due to differential cell surface levels. We transfected 293T cells, which lack ACE2 and thus do not fuse upon S

expression, with the different variant plasmids and assessed S surface levels by flow cytometry. The variants S proteins were equally expressed after transfection **(Fig. EV4A-B).**

We then measured the kinetics of syncytia formation induced by the different S proteins in the Vero GFP Split cells. We conducted a comparative video-microscopy analysis where cell-cell fusion could be visualized as soon as 6h post-transfection. The fusion kinetics of B.1.1.7 S protein was more rapid than any of the other variants **(Fig. 3C and Movie E1)**. B.1.351 also induced significantly faster fusion than D614G, whereas the Wuhan S was the slowest of all the compared proteins **(Fig. 3C and Movie E1)**. Thus, B.1.1.7 and B.1.351 S protein are more potent fusogens than either the D614G or Wuhan strains.

We previously reported that IFITMs restrict Wuhan S mediated cell-cell fusion and that their activity was counteracted by the TMPRSS2 protease (Buchrieser *et al.*, 2020). As infection with B.1.1.7 and B.1.351 induce more syncytia, we further investigated if this resulted in an increased resistance to IFITM restriction. We thus characterized the impact of IFITMs on syncytia formed by expression of D614G, B.1.1.7 and B.1.351 S proteins. The variants were effectively restricted by IFITMs **(Fig. EV5A-E)**. The presence of TMPRSS2 increased fusion of all S proteins and reverted the restriction by IFITMs **(Fig. EV5A-E)**. Taken together, our data show that B.1.1.7 and B.1.351 variants induce more syncytia, but that their S proteins remain similarly sensitive to IFITMs.

178 **Contribution of individual variant-associated mutations on Spike fusogenicity.**

179 We next sought to determine the contribution of each variant-associated mutation to
180 cell-cell fusion. Both B.1.1.7 and B.1.351 S proteins contain the N501Y mutation in the RBD and
181 the D614G mutation in the S1/S2 cleavage site **(Fig. 4A).** B.1.1.7 S contains the Δ69/70 and
182 ΔY144 deletions in the N-terminal domain (NTD), P681H and T716I mutations in the S1/S2
183 cleavage site, the S982A mutation in the heptad repeat 1 (HR1) site and the D1118H mutation
184 in between HR1 and HR2. The B.1.351 S is comprised of the L18F, D80A, D215G and Δ242-244
185 mutations in the NTD, K417N and E484K mutations in the receptor binding domain (RBD), and
186 A701V in the S1/S2 cleavage site. We introduced individual mutations into the D614G
187 background. Following reports of the emergence of the E484K mutation within the B.1.1.7
188 variant (Collier *et al*, 2021), we also generated a mutant B.1.1.7 S protein with the E484K
189 mutation. We observed by flow cytometry that the mutant S proteins were similarly expressed
190 at the cell surface **(Fig. EV4 C and EV6 A-D)**. We expressed each mutant into Vero GFP split and
191 measured their potential to induce cell-cell fusion in comparison to D614G S protein.

192 Of the mutations that are associated with B.1.1.7, we found that the Δ69/70 deletion in
193 the RBD decreased cell-cell fusion whereas P681H and D1118H substitutions both increase
194 fusion **(Fig. 4A and EV6G)**. P681H displayed the greatest fusogenicity of all investigated
195 mutations, being almost 2.5-fold higher than D614G S **(Fig. 4A and EV6G).** As previously
196 mentioned, the introduction of the D614G mutation in the S1/S2 boarder of the Wuhan S
197 protein also relatively increased fusion, stressing the importance of this cleavage site in
198 determining fusogenicity **(Fig. 3B)**.

Among the mutations associated with B.1.351, the Δ242-244 deletion as well as K417N and E484K mutations in the RBD significantly decreased syncytia formation **(Fig. 4A and EV6H)**. Only the D251G mutation in the NTD modestly increased syncytia formation relative to D614G **(Fig. 4A and EV6H)**. The introduction of the E484K RBD mutation into the B.1.1.7 S protein significantly decreased its potential to form syncytia, despite not changing cell surface expression, further supporting the mutation's restrictive effect on cell-cell fusion **(Fig. 4B and EV4C)**. Taken together, our data suggests that the variant S proteins are comprised of mutations that play contrasting roles in cell-cell fusion. P681H, D1118H, and D215G substitutions facilitate fusion, whereas mutations Δ69/70, Δ242-244, K417N, and E484K antagonize cell-cell fusion.

Binding of Spike proteins bearing individual variant-associated mutations to ACE2.

We next explored the impact of variant-associated mutations on S binding to the ACE2 receptor. To this aim, we transiently expressed each mutant protein in 293T cells. Cells were then stained with a serial dilution of soluble biotinylated ACE2, revealed with fluorescent streptavidin and then analyzed by flow cytometry **(Fig. 5A)**. Titration binding curves were generated and EC50 (the amount of ACE2 needed for 50% binding) was calculated. The S protein of B.1.1.7 had the highest affinity to ACE2, confirming previous results by us and others (Planas *et al.*, 2021)(Ramanathan *et al*, 2021). B.1.1.7 was sequentially followed by B.1.351, D614G, and Wuhan S **(Fig. 5B and EV7A)**. As expected, mutations within the RBD had the most significant impact on ACE2 binding. N501Y found in both B.1.1.7 and B.1.351 drastically

increased ACE2 binding, in line with previous reports indicating that this mutation enhances affinity of the viral protein to its receptor (Ali *et al*, 2021; Luan *et al*, 2021; Tian *et al*, 2021). The K417N substitution present in the B.1.351 S decreased ACE2 binding **(Fig. 5B and EV7C)**. The E484K mutant had a slightly, but not significantly, higher binding to ACE2 **(Fig. EV7C)**. This was corroborated by the observation that addition of the E484K mutation to B.1.1.7 S protein also slightly increased ACE2 binding **(Fig. 5B and EV7A)**. Mutation in the S1/S2 cleavage site, HR1/HR2 sites or NTD did not have any significant impact on ACE2 binding **(Fig. 5B and EV7B-E)**. It is worth noting that the NTD Δ242-244 mutant displayed a marginally lower binding to ACE2 **(Fig. 5B and EV7B)**. Therefore, the N501Y mutation is the single most significant contributor to increased ACE2 binding of the variants, though it does not affect cell-cell fusion on its own. The K417N, Δ242-244, and E484K mutations restrict fusogenicity but differently effect ACE2 binding; with the former two decreasing affinity and the latter slightly increasing.

Therefore, ACE2 binding and fusogenicity are two functions of the S protein that can be partially deconvoluted through individual mutations.

Antibody binding to Spike proteins bearing individual variant-associated mutations.

We then investigated if variant associated mutations that modulate fusogenicity arose in the context of antibody escape. To this aim, we assessed by flow cytometry the binding of a panel of four human monoclonal antibodies (mAbs) to the different S mutants. As a control we used mAB10, a pan-coronavirus antibody that targets an unknown but conserved epitope

240 within the S2 region (Planchais, manuscript in preparation). mAb10 equally recognized all
241 variants and associated individual mutations **(Fig. 5C)**. mAb48 and mAb98 target the RBD and
242 mAb71 the NTD (Planchais, manuscript in preparation). mAb48 did not recognize the B.1.351
243 variant, and more specifically did not bind to the K417N mutant **(Fig. 5C)**. The mAb71
244 recognized neither B.1.1.7 nor B.1.351 variants and did not bind to their respective NTD ΔY144
245 and Δ242-244 mutations. The K417N and Δ242-244 mutations were also responsible for
246 decreasing S-mediated fusion, suggesting a tradeoff between antibody escape and fusion **(Fig.**
247 **5C)**. mAb98 did not recognize the B.1.351 variant. However, none of the associated mutations
248 were specifically responsible for the lack of binding **(Fig. 5C)**, suggesting a combined effect on
249 the structure of the S protein that may affect antibody escape.

250

251 **Discussion**

252 The replication and cytopathic effects of SARS-CoV-2 variants is under intense scrutiny,
253 with contrasting results in the literature (Frampton *et al.*, 2021; Hou *et al*, 2020; Leung *et al*,
254 2021; Liu *et al*, 2021b; Touret *et al.*, 2021). For instance, there was no major difference in the
255 replication kinetics of B.1.1.7 and D614G strains in some reports (Thorne *et al*, 2021; Touret *et*
256 *al.*, 2021), whereas others suggested that B.1.1.7 may outcompete D614G in a co-infection
257 assay (Touret *et al.*, 2021). Other studies proposed that the N501Y mutation may provide a
258 replication advantage, whereas others suggested that N501Y is deleterious (Frampton *et al.*,
259 2021; Hou *et al.*, 2020; Leung *et al.*, 2021; Liu *et al.*, 2021b). These discrepant results may be

due to the use of different experimental systems, viral strains, multiplicities of infection and cell types.

Here, we show that variants replicate to the same extent as the early D614G strain in different human cell lines and primary airway cells. Moreover, B.1.1.7 and B.1.351 induced more cell-cell fusion than D614G. Increased fusion was observed in U2OS-ACE2 cells and in naturally permissive Vero cells. In agreement with infection data, transfection of B.1.1.7 and B.1.351 S proteins, in the absence of any other viral factors, produced significantly more syncytia than D614G, which in turn, fused more than the Wuhan S. Comparative video microscopy analysis revealed that the B.1.1.7 S fused the most rapidly, which was then followed by B.1.351, D614G, and finally Wuhan. Thus, B.1.1.7 and B.1.351 variants display enhanced S-mediated syncytia formation.

We further show that B.1.1.7 and B.1.351 remain sensitive to restriction by IFN-β1. The fusion mediated by their respective S proteins is inhibited by IFITMs. This extend previous results by us and others demonstrating that ancestral Wuhan S is effectively inhibited by this family of restriction factors (Buchrieser *et al.*, 2020; Shi *et al.*, 2021). It has been recently reported that B.1.1.7 may lead to lower levels of IFN-β1 production by infected Calu-3 cells and may be less sensitive to IFN-β pre-treatment, when compared to first wave viral isolates (Thorne *et al.*, 2021). We did not detect here differences of IFN-β1 sensitivity between the variants in Vero and U2OS-ACE2 cells. Again, these discrepant results may reflect inherent differences between Calu-3, Vero and U2OS-ACE2 cells, or the use of different viral isolates.

We then characterized the contribution of the individual mutations present in the B.1.1.7 and B.1.351 S proteins to their respective fusogenicity. The highly fusogenic B.1.1.7 S consists of more mutations that robustly increase fusion (P681H and D1118H) than mutations that decrease fusion (Δ69/70). In contrast, the B.1.351 variant is comprised of several restrictive mutations (Δ242-244, K417N, and E484K) and only one mutation that modestly increased fusion (D215G). The strongest increase in fusion was elicited by the P681H mutation at the S1/S2 border. This mutation likely facilitates proteolytic cleavage of S and thus promotes S mediate cell-cell fusion. Indeed, the analogous P681R mutation present in B.1.617.2 and B.1.617.3 variants increases S1/S2 cleavage and facilitates syncytia formation (Ferreira *et al*, 2021; Jiang *et al*, 2020). Of note, another report with indirect assessment of variant S fusogenicity suggested a mild decrease or no difference in cell-cell fusion of B.1.1.7 and B.1.351 relative to Wuhan S (Hoffmann *et al*, 2021). These previous experiments were performed in 293T cells at a late time-points (24 hours post-transfection), which may preclude detection of an accelerated fusion triggered by the variants.

We show that the binding of variant S to soluble ACE2 paralleled their fusogenicity. B.1.1.7 bound the most efficiently to ACE2, followed by B.1.351, D614G and finally Wuhan. However, the ACE2 affinity of S proteins carrying individual mutations did not exactly correlate to fusogenicity. For instance, the N501Y and D614G mutations drastically increased ACE2 affinity, but only D614G enhanced fusogenicity. The K417N substitution, and to a lesser degree Δ242-244, had a lower affinity to ACE2 and also restricted cell-cell fusion. The E484K mutation significantly restricts fusion, but mildly increases ACE2 affinity. This suggests that on the level of

individual S mutations, the relationship between ACE2 affinity and increased fusogenicity is not always linear.

We selected a panel of 4 mAbs that displayed different profiles of binding to B.1.1.7, B.1.351, D614G and Wuhan S proteins. The mAb10 targeting the S2 domain recognized all variants and was used as a positive control. Wuhan and D614G were recognized by the three other antibodies, targeting either the NTD or RBD. B.1.1.7 lost recognition by the anti-NTD mAb71, whereas B.1.351 was neither recognized by mab71 nor by the two anti-RBD antibodies mAb48 and mAb 98. Upon examining the potential of S proteins carrying individual mutations to bind to human monoclonal antibodies, we found that the ones that restrict (Δ242-244, K417N) or have no effect on fusogenicity (ΔY144) are also not recognized by some mAbs. This suggests that variant S proteins have undergone evolutionary trade off in some circumstances; selecting for mutations that provide antibody escape at the detriment of fusogenicity. In accordance with our findings, deep sequence binding analysis and in vitro evolution studies suggest the N501Y mutation increases affinity to ACE2 without disturbing antibody neutralization (Liu *et al*, 2021a; Starr *et al.*, 2021; Zahradník *et al*, 2021). The E484K and K417N RBD mutations in the B.1.351 variant may also increase ACE2 affinity, particularly when in conjunction with N501Y (Zahradník *et al.*, 2021) (Nelson *et al*, 2021). However, the resulting conformational change of the S protein RBD may also decrease sensitivity to neutralizing antibodies (Nelson *et al.*, 2021). Future work assessing the structural and conformational changes in the S protein elicited by a combination of individual mutations or deletions may further help elucidate the increased fusogenicity and antibody escape potential of the variants.

The presence of infected syncytial pneumocytes was documented in the lungs of patients with severe COVID-19 (Bussani *et al.*, 2020; Tian *et al*, 2020; Xu *et al*, 2020). Syncytia formation may contribute to SARS-CoV-2 replication and spread, immune evasion and tissue damage. A report using reconstituted bronchial epithelia found that viral infection results in the formation and release of infected syncytia that contribute to the infectious dose (Beucher *et al*, 2021). The neutralizing antibody response to SARS-CoV-2 infection has divergent effect on cell-cell fusion, with some antibodies restricting S mediated fusion, while other increase syncytia formation (Asarnow *et al*, 2021). Cell-to-cell spread of virus may be less sensitive to neutralization by monoclonal antibodies and convalescent plasma than cell-free virus (Jackson *et al*, 2021). It is thus possible that infected syncytial cells facilitate viral spread. Heterocellular syncytia containing internalized lymphocytes have also been detected in infected lung tissue (Zhang *et al*, 2021). The targeting of lymphocytes for cell-in-cell mediated death suggest that syncytia may contribute to immune escape (Zhang *et al.*, 2021). Within this context, it is necessary to better understand the fusogenic potential of the SARS-CoV-2 variants that have arisen and will continue to emerge.

We have characterized here the replication, fusogenicity, ACE2 binding and antibody recognition of B.1.1.7 and B.1.351 variants and the role of their S-associated mutations. Despite the insights we provide into the S-mediated fusogenicity of the variants, we did not address the conformational changes that the mutations individually or in combination may elicit. We show that B.1.1.7 more efficiently binds to ACE2 and is more fusogenic than B.1.351. Whether these two features of B.1.1.7 explain its higher transmissibility rate than B.1.351 will deserve further

investigation. It will be also of interest to similarly characterize the variants that are continuously arising, including B.1.617.2, which represents a growing threat worldwide.

Material and Methods

Plasmids

A codon optimized version of the reference Wuhan SARS-CoV-2 Spike (GenBank: QHD43416.1) was ordered as a synthetic gene (GeneArt, Thermo Fisher Scientific) and was cloned into a phCMV backbone (GeneBank: AJ318514), by replacing the VSV-G gene. The mutations for B.1.1.7 and B.1.351 (**Fig. 4A**) were added in silico to the codon-optimized Wuhan strain and ordered as synthetic genes (GeneArt, Thermo Fisher Scientific) and cloned into the same backbone (Planas *et al.*, 2021a). The D614G S-protein was generated by introducing the mutation into the Wuhan reference strain via Q5 Site-directed mutagenesis (NEB). Other individual mutations were subsequently introduced into the D614G S by the same process. Plasmids were sequenced prior to use. The primers used for sequencing and the site-directed mutagenesis are presented in the supplement **(EV Tables 1 and 2)**. pQCXIP-Empty control plasmid, pQCXIP-IFITM1-N-FLAG, pQCXIP-IFITM2-N-FLAG, pQCXIP-IFITM3-N-FLAG were

362 previously described (Buchrieser *et al*, 2019). pQCXIP-BSR-GFP11 and pQCXIP-GFP1-10 were
363 from Yutaka Hata ((Kodaka *et al*, 2015); Addgene plasmid #68716;
364 http://n2t.net/addgene:68716; RRID: Addgene_68716 and Addgene plasmid #68715;
365 http://n2t.net/addgene:68715; RRID: Addgene_68715). pcDNA3.1-hACE2 was from Hyeryun
366 Choe ((Li *et al*, 2003); Addgene plasmid # 1786; http://n2t.net/addgene:1786; RRID:
367 Addgene_1786). pCSDest-TMPRSS2 was from Roger Reeves ((Edie *et al*, 2018); Addgene
368 plasmid # 53887; http://n2t.net/addgene:53887; RRID: Addgene_53887).

369 **Cells**

370 Vero E6, HEK293T, U2OS, Caco2/TC7, Calu3 were cultured in DMEM with 10% Fetal Bovine
371 Serum (FBS) and 1% Penicillin/Streptomycin (PS). Vero and 293T GFP-split cells transduced cells
372 with pQCXIP were cultured with 4ug/ml and 1 ug/ml of puromycin (InvivoGen), respectively.
373 U2OS GFP-split cells transduced with pLenti6 were cultured in 1ug/ml puromycin and 10 ug/ml
374 blasticidin (InvivoGen). The MucilAir^{TM} primary human bronchial epithelial model was
375 previously described (Robinot *et al.*, 2020). All cells lines were either purchased from ATCC or
376 were kind donations from members of the Institut Pasteur and were routinely screened for
377 mycoplasma.

378

379 **Viruses**

380 The Wuhan SARS-CoV-2 strain (BetaCoV/France/IDF0372/2020) and the D614G strain (hCoV-
381 19/France/GE1973/2020) was supplied by Dr. S. van der Werf of the National Reference Centre

for Respiratory Viruses (Institut Pasteur, Paris, France). The D614G viral strain was sourced through the European Virus Archive goes Global (EVAg) platform, which is funded by the European Union's Horizon 2020 research and innovation program under grant agreement 653316. The B.1.1.7 strain was isolated in Tours, France, from an individual who returned from the United Kingdom. The B.1.351 strain (CNRT 202100078) originated from an individual in Creteil, France). Informed consent was provided by the individuals for use of their biological materials. The viruses were isolated from nasal swabs on Vero cells and further amplified one or two passages on Vero cells. The viruses were sequenced directly from the nasal squabs and again upon passaging. Titration of Viral stocks was performed by 50% tissue culture infectious dose (TCID50).

Viral Release

For quantification of extracellular viral RNA, supernatants were diluted and heat-inactivated for 20min at 80°C. qRT-PCR was performed from 1µL of template RNA in a final volume of 5 µL per reaction in 384-well plates using the Luna Universal Probe One-Step RT-qPCR Kit (New England Biolabs) with SARS-CoV-2 N-specific primers (**EV Table 1)** on a QuantStudio 6 Flex thermocycler (Applied Biosystems). Standard curve was performed in parallel using purified SARS-CoV-2 viral RNA. Infectious virus release was assessed by harvesting supernatant at each time point and preforming a TCID50 assay using Vero cells.

GFP-Split Fusion assay

For cell-cell fusion assays, Vero, U2OS-ACE2, or 293T cell lines stably expressing GFP1-10 and GFP11 were co-cultured at a 1:1 ration ($3x10^4$, $7x10^4$, and $2x10^4$ cells/well total, respectively) were transfected in suspension with a total of 100ng of DNA with Lipofectamine 2000 (Thermo) in a 96 well plate (uClear, #655090). 10 ng of phCMV-SARS-CoV2-S and/or 25 ng of pCDNA3.1-hACE2, 25 ng of pCSDest-TMPRSS2, and 40 ng of pQCXIP-IFITM were used and adjusted to 100 ng DNA with pQCXIP-Empty. At 20 h post-transfection images covering 80-90% of the well surface, were acquired per well on an Opera Phenix High-Content Screening System (PerkinElmer). The GFP area and the number of nuclei was quantified on Harmony High-Content Imaging and Analysis Software **(Fig EV2B).** For infection, cells were plated at the aforementioned concentrations and infected the next day with a range of MOIs and fixed at 20h (U2OS-ACE) or 48h (Vero) post-infection with 4% paraformaldehyde for 30mins. For video microscopy experiments, Vero GFP split cells (mixed 1:1) were transfected in suspension with 50ng of phCMV-SARS-CoV2-S and 450ng of pQCXIP-Empty for 30mins at 37°C. Cells were washed twice and then seeded at a confluency of $2x10^5$ cells per quadrant in a u-Dish 35mm Quad dish (ibidi-#80416). Cells were allowed to settle, and fluorescence images were taken at 37°C every 10min up to 24h using a Nikon BioStation IMQ, with three fields for each condition. Fusion defined as percent of GFP pixels was calculated with ImageJ.

Flow cytometry

For ACE2 binding, 293T cells transfected with S proteins for 24h were stained with soluble biotinylated ACE2 diluted in MACS Buffer at indicated concentrations (from 60 to 0.01 µg/mL) for 30 min at 4°C. The cells were then washed twice with PBS and then incubated with Alexa Fluor 647- conjugated-streptavidin (Thermo Fisher Scientific, 1:400) for 30 min at 4°C. Finally, the cells were washed twice with PBS and then fixed with 4% paraformaldehyde. The results were acquired using an Attune Nxt Flow Cytometer (Life Technologies). Transfection efficiency was assessed by staining with pan-SARS-CoV-2 human mAb129. Antibody binding to S proteins was assessed via s analogous protocol where transfected 293T cells were first stained with either human mAb10 (pan-coronavirus anti-S2), mAb102 and mAB129 (pan-SARS-CoV-2), mAb48 and mAb98 (SARS-CoV-2 anti-RBD), and mAb71 (SARS-CoV-2 anti-NTD) at 1 µg/mL. For viral replication, infected cells were fixed at each time with 4% paraformaldehyde for 30mins. The cells were stained in the same manner described above with anti-spike mAb102 and secondary Alexa Fluor 647 (1:500) in MACS buffer containing 0.05% saponin. The gating strategy to determine spike positive cells is represented in the supplement **(Fig EV1B)**.

Statistical analysis

Flow cytometry data was analyzed with FlowJo v10 software (Tristar). Calculations were all performed with Microsoft Excel 365. GraphPad Prism 9 was used to generate figure and for statistical analysis. Statistical significance between different conditions was calculated using the tests indicated in the corresponding figure legends.

Acknowledgments

We thank members of the Virus and Immunity Unit for helpful discussions. Nathalie Aulner and the UtechS Photonic BioImaging (UPBI) core facility (Institut Pasteur), a member of the France BioImaging network, for image acquisition and analysis support. Work in OS lab is funded by Institut Pasteur, Urgence COVID-19 Fundraising Campaign of Institut Pasteur, ANRS, the Vaccine Research Institute (ANR-10-LABX-77), Fondation Pour la Recherche Médicale (FRM), Labex IBEID (ANR-10-LABX62-IBEID), ANR/FRM Flash Covid PROTEO-SARS-CoV-2 and IDISCOVR. Work in UPBI is funded by grant ANR-10-INSB-04-01 and Région Ile-de-France program DIM1-Health. MMR and MZ are supported by the Pasteur-Paris University (PPU) International Doctoral Program. DP is supported by the Vaccine Research Institute. LG is supported by the French Ministry of Higher Education, Research and Innovation. EB is supported by the Medecine-Sciences ENS-PSL Program. HM lab is funded by the Institut Pasteur, the Milieu Intérieur Program (ANR-10-LABX-69- 01), the INSERM, REACTing, EU (RECOVER) and Fondation de France (#00106077) grants. The funders of this study had no role in study design, data collection, analysis, interpretation, or the writing of the article.

Author contributions

Experimental strategy and design: MMR, JB, MH, LG, RR, LC, OS.

Experimentation: MMR, JB, MH, EB, RR, NS, LG, FGB, FP, RR.

Vital materials and expert advice: CP and HM.

Data processing and figure generation: MMR.

Manuscript writing and editing MMR, JB, OS.

Supervision: JB and OS.

All authors reviewed and approved the manuscript,

Conflict of interests: C.P, H.M and O.S have a pending patent application for the anti-RBD mAbs described in the present study (PCT/FR2021/070522).

Figure Legends

Figure 1. Replication kinetics of D614G, B.1.1.7 and B.1.351 variants in cell culture. Cells were infected at the indicated MOI. Viral replication (Left) and release (Right) were assessed by flow cytometry and RT-qPCR. **A)** Caco2/TC7 cells **B)** Calu-3 cells **C)** Vero cells **D)** primary human airway epithelial cells virus release (Right) and infectious virus release (Left). Data are mean ± SD of at least 3 independent experiments. Statistical analysis: Mixed-effect analysis or Two-way ANOVA compared to D614G reference, ns: non-significant, *P < 0. 05, **P < 0.01, ***P < 0.001, ****P < 0.0001.

Figure 2. SARS-CoV-2 variant infection increases formation of syncytia in U2OS-ACE2 and Vero GFP-split cells. **(A)** U2OS-ACE2 or Vero cells expressing either GFP 1-10 or GFP 11 (1:1 ratio) were infected 24h after plating and imaged 20h (U2OS-ACE2) or 48h (Vero) post-infection. **(B) Left Panel:** Fusion was quantified by GFP area/ number of nuclei and normalized to D614G for U2OS-ACE2 20h post infection at MOI 0.001. **Right Panel:** Representative images of U2OS-ACE2 20h post infection, GFP-Split (Green) and Hoechst (Blue). Top and bottom are the same images with and without Hoechst channel. **(C) Left Panel:** Quantified fusion of Vero cells infected at MOI 0.01. **Right Panel:** Representative images of Vero cells 48h post infection, GFP-Split (Green) and Hoechst (Blue). Scale bars: 200 µm. Data are mean ± SD of 8 independent

experiments. Statistical analysis: One-way ANOVA compared to D614G reference, ns: non-significant, *P < 0. 05, **P < 0.01, ***P < 0.001, ****P < 0.0001.

Figure 3. B.1.17 and B.1.351 SARS-CoV-2 Spike proteins induce more robust syncytia formation. (A) Vero GFP-split cells were transfected with variant spike proteins and imaged 18h post-transfection. **(B) Left Panel**: Fusion was quantified by GFP area/ number of nuclei and normalized to D614G for each of the transfected variant spike proteins. **Right Panel**: Representative images of Vero GFP-split cells 18h post-transfection, GFP (Green) and Hoechst (Blue). Top and bottom are the same images with and without Hoechst channel. **(C) Left Panel**: Quantification of variant spike mediated fusion in Vero-GFP split cells by video microscopy. Results are mean ± SD from three fields per condition from one representative experiment. **Right Panel**: Fusion quantification of at least 3 independent video microscopy experiments, 20h post transfection, normalized to D614G. Scale bars: 200 µm. Data are mean ± SD of at least 3 independent experiments. Statistical analysis: One-way ANOVA compared to D614G reference, ns: non-significant, *P < 0. 05, **P < 0.01, ***P < 0.001, ****P < 0.0001.

Figure 4. Mutations associated with B.1.1.7 and B.1.351 Spike proteins differentially affect cell-cell fusion. (A) Schematic representation of the S protein colour coded for the functional regions: N-terminal domain (NTD), receptor binding domain (RBD), fusion peptide (FP), heptad repeat 1,2 (HR1, HR2), transmembrane anchor (TA), C-terminal domain (CTD). **(B) Left Panel:**

Vero GFP-split cells were transfected with spike plasmids containing each of the individual mutations associated with B.1.1.7 variant in the D614G background. The amount of fusion was quantified at 20h and normalized to D614G reference plasmid. Colour code of each mutation corresponds to spike functional regions represented in (A). **Right Panel:** Quantified fusion for each of the individual spike mutations associated with B.1.351. Data set for N501Y and D614G reference mutations are duplicated between left and right panels for presentation as mutations are common to both variants. **(C) Left Panel:** Quantified fusion of the B.1.1.7 + E484K variant S protein normalized to D614G S. **Right Panel:** Representative images of fusion at 20h. Scale bar: 200 µm. Data are mean ± SD of at least 4 independent experiments. Top and bottom are the same images with and without Hoechst channel. Statistical analysis: statistics for both left and right panels of A were conducted together. One-way ANOVA compared to D614G reference, ns: non-significant, *P < 0. 05, **P < 0.01, ***P < 0.001, ****P < 0.0001.

Figure 5. ACE2 and monoclonal antibody binding to Spike proteins with B.1.1.7 and B.1.351 associated mutations. **(A)** 293T cells were transfected Spike proteins with each variant-associated mutation for 24h and stained with biotinylated ACE2 and fluorescent streptavidin before analysis by flow cytometry. **(B) Left Panel:** EC50 values (concentration of ACE2 needed for 50% binding) for B.1.1.7 and associated mutations. Colour code corresponds to location on spike functional domains and lower EC50 values signifies higher affinity to ACE2 binding. **Right Panel:** EC50 values for B.1.351 and associated mutations. Data set for N501Y and D614G reference mutations are duplicated between left and right panels as mutations are common to

both variants. **(C)** Spike transfected 293T cells were stained with human monoclonal antibodies targeting the S2 (mAb10), RBD (mAb48 and mAb98), and the NTD (mAb71). Cells were analyzed by flow cytometry. The percentage of positive cells is indicated. Data are mean of at least 3 independent experiments. Statistical analysis: One-way ANOVA compared to D614G reference, ns: non-significant, *P < 0. 05, **P < 0.01, ***P < 0.001, ****P < 0.0001.

Figure EV1. SARS-CoV-2 variant infection at different MOIs and inhibition by IFN-β1. (A) Caco-2/TC7 (left), Calu-3 (middle), and Vero cells (right) were infected at the indicated MOIs with SARS-CoV-2 variants for 24h. The number of spike protein positive cells was determined by flow cytometry upon staining with human pan-SARS-CoV-2 mAb102. Only MOIs that were not saturating were used to generate replication curves for each cell line studied. **(B)** Representative image of gating strategy used for flow cytometry to determine spike positive cells. **(C)** Vero cells were pre-treated for 2h with a serial dilution of IFN-β1 prior to infection with the SARS-CoV-2 variants. Infected cells were maintained in media containing IFN-β1 and analyzed by flow cytometry 48h post-infection to determine relative infection change.

Figure EV2. Qualitative and quantitative assessment of syncytia formation

(A) U2OS-ACE2 GFP-split cells were infected at MOI 0.01 with the Wuhan, D614G, B.1.1.7 and B.1.351 strains for 20h. Cells were stained for spike protein with the human pan-SARS-CoV-2

102 mAb and Alex647 fluorescent secondary antibody. Representative confocal images of the variant induced syncytia formation: GFP-Split (Green), Spike (red) and Hoechst (Blue). **(B)** Quantification method for syncytia formation using the Opera Phenix high content imager and harmony software: Total syncytia area (GFP area) is normalized for cell number upon quantifying the number of nuclei (Hoechst). Scale bars: 50 µm

Figure EV3. Syncytia formation by SARS-CoV-2 variants at high MOIs and restriction by IFN-β1. **(A) Left Panel:** Fusion normalized to D614G for U2OS-ACE2 20h post infection at MOI 0.01. **Right Panel:** Representative images of U2OS-ACE2 20h post infection, GFP (Green) and Hoechst (Blue). Top and bottom are the same images with and without Hoechst channel. **(B) Left Panel:** Quantified fusion of Vero cells infected at MOI 0.1. **Right Panel:** Representative images of Vero cells 48h post infection. **(C)** U20S-ACE2 GFP split cells were pre-treated for 2h with a serial dilution of IFN-β1 prior to infection with the SARS-CoV-2 variants. Infected cells were maintained in media containing IFN-β1 and relative inhibition of syncytia formation 20h post-infection was determined via GFP signal. Scale bars: 200 µm. Data are mean ± SD of at least 3 independent experiments. Statistical analysis: One-way ANOVA compared to D614G reference, ns: non-significant, *P < 0. 05, **P < 0.01, ***P < 0.001, ****P < 0.0001.

Figure EV4. SARS-CoV-2 variant Spikes are expressed equally at the cell surface. 293T cells were transfected with variant S proteins for 20h and stained with human pan-coronavirus mAb10 without permeabilization. 293T cells were chosen because they lack ACE2 and do not

fuse upon S transfection; this makes them suitable for single cell flow cytometry **(A) Left Panel:** Quantification of percent of cells expressing each spike at the surface. **Right Panel:** Representative FACs plots. **(B) Left Panel:** Quantification of median florescent intensity (MFI) of variant spikes at the cell surface. **Right Panel:** Representative histograms of MFI of each variant spike. Data are mean ± SD of at least 3 independent experiments. **(C) Left Panel:** Representative FACs plots for B.1.1.7 + E484K spike. **Right Panel:** Representative MFI histogram for B.1.1.7 + E484K spike. Statistical analysis: One-way ANOVA compared to D614G reference, ns: non-significant, *P < 0. 05, **P < 0.01, ***P < 0.001, ****P < 0.0001.

Figure EV5. SARS-CoV-2 variant Spike mediated cell-cell fusion is equally restricted by IFITMs.

(A) A co-culture of 293T GFP-Split cells were transfected with combination of S, control, ACE2, TMPRSS2 and IFITM plasmids and then imaged 18h post-transfection. Effect of IFITMs and TMPRSS2 on the cell-cell fusion induced by different spike proteins **(B)** Wuhan **(C)** D614G **(D)** B.1.1.7 **(E)** B.1.351. Data are mean ± SD of at least 3 independent experiments. Statistical analysis: One-way ANOVA compared to D614G reference or control plasmid transfection, ns: non-significant, *P < 0. 05, **P < 0.01, ***P < 0.001, ****P < 0.0001.

Figure EV6. SARS-CoV-2 variant spike associated mutations are expressed equally at the cell surface. 293T cells were transfected with S proteins with each of the variant associated mutations for 18h and stained with human pan-coronavirus mAb10 without permeabilization. **(A)** Representative FACs plots of percent of cells expressing each mutant spike at the surface.

(B) Quantification of percent of cells expressing each spike at the surface. **(C)** Quantification of median florescent intensity (MFI) of the mutant spikes at the cell surface. **(D)** Representative histograms of MFI of each mutant spike. **(E)** Representative images of Vero GFP split cells 20h after transfection with each B.1.1.7 variant associated mutant spike, GFP-Split (Green). **(F)** Representative images of Vero GFP split cells 20h after transfection with each B.1.351 variant associated mutant spike.

Statistical analysis: One-way ANOVA compared to D614G reference, ns: non-significant, *P < 0.05, **P < 0.01, ***P < 0.001, ****P < 0.0001.

Figure EV7. ACE2 binding curves to SARS-CoV-2 variant Spikes and associated mutations. 293T cells were transfected with variant or mutant spike proteins for 24h and stained with a serial dilution of soluble biotinylated ACE2 and revealed by fluorescent streptavidin before analysis by flow cytometry. **(A)** ACE2 binding dilution curves of each variant spike. **(B)** ACE2 binding dilution curves of each variant associated mutation located in spike n-terminal domain (NTD) **(C)** receptor binding domain (RBD) **(D)** S1/S2 cleavage site **(E)** heptad repeat 1-2 site (HR1-HR2). Data are mean ± SD of 3 independent experiments.

Movie EV1: B.1.17 and B.1.351 Spike proteins induce more robust syncytia formation than D614G or Wuhan

A co-culture of Vero GFP-split cells were transfected with plasmids expressing each of the variant spike proteins and imaged by video microscopy at a rate of 6 images per hour for 24h. GFP signal is superimposed over BF images. The white border represents the GFP area calculated by the ImageJ macro in order to quantify fusion. **Top left:** Wuhan S **Top right:** D614G S **Bottom Left:** B.1.1.7 S **Bottom right:** B.1.351. One representative field for each condition is shown.

References

Ali F, Kasry A, Amin M (2021) The new SARS-CoV-2 strain shows a stronger binding affinity to ACE2 due to N501Y mutant. *Med Drug Discov* 10: 100086

Arunachalam PS, Wimmers F, Mok CKP, Perera R, Scott M, Hagan T, Sigal N, Feng Y, Bristow L, Tak-Yin Tsang O *et al* (2020) Systems biological assessment of immunity to mild versus severe COVID-19 infection in humans. *Science* 369: 1210-1220

Asarnow D, Wang B, Lee WH, Hu Y, Huang CW, Faust B, Ng PML, Ngoh EZX, Bohn M, Bulkley D *et al* (2021) Structural insight into SARS-CoV-2 neutralizing antibodies and modulation of syncytia. *Cell*

Bastard P, Orlova E, Sozaeva L, Levy R, James A, Schmitt MM, Ochoa S, Kareva M, Rodina Y, Gervais A *et al* (2021) Preexisting autoantibodies to type I IFNs underlie critical COVID-19 pneumonia in patients with APS-1. *J Exp Med* 218

Bastard P, Rosen LB, Zhang Q, Michailidis E, Hoffmann HH, Zhang Y, Dorgham K, Philippot Q, Rosain J, Beziat V *et al* (2020) Autoantibodies against type I IFNs in patients with life-threatening COVID-19. *Science* 370

Beucher G, Blondot M-L, Celle A, Pied N, Recordon-Pinson P, Esteves P, Faure M, Métifiot M, Lacomme S, Dacheaux D *et al* (2021) SARS-CoV-2 transmission via apical syncytia release from primary bronchial epithelia and infectivity restriction in children epithelia. *bioRxiv*: 2021.2005.2028.446159

Braga L, Ali H, Secco I, Chiavacci E, Neves G, Goldhill D, Penn R, Jimenez-Guardeno JM, Ortega-Prieto AM, Bussani R *et al* (2021) Drugs that inhibit TMEM16 proteins block SARS-CoV-2 spike-induced syncytia. *Nature*

Buchrieser J, Degrelle SA, Couderc T, Nevers Q, Disson O, Manet C, Donahue DA, Porrot F, Hillion KH, Perthame E *et al* (2019) IFITM proteins inhibit placental syncytiotrophoblast formation and promote fetal demise. *Science* 365: 176-180

Buchrieser J, Dufloo J, Hubert M, Monel B, Planas D, Rajah MM, Planchais C, Porrot F, Guivel-Benhassine F, Van der Werf S *et al* (2020) Syncytia formation by SARS-CoV-2-infected cells. *EMBO J* 39: e106267

Buss LF, Prete CA, Jr., Abrahim CMM, Mendrone A, Jr., Salomon T, de Almeida-Neto C, Franca RFO, Belotti MC, Carvalho M, Costa AG *et al* (2021) Three-quarters attack rate of SARS-CoV-2 in the Brazilian Amazon during a largely unmitigated epidemic. *Science* 371: 288-292

Bussani R, Schneider E, Zentilin L, Collesi C, Ali H, Braga L, Volpe MC, Colliva A, Zanconati F, Berlot G *et al* (2020) Persistence of viral RNA, pneumocyte syncytia and thrombosis are hallmarks of advanced COVID-19 pathology. *EBioMedicine* 61: 103104

Chan JF, Chan KH, Choi GK, To KK, Tse H, Cai JP, Yeung ML, Cheng VC, Chen H, Che XY *et al* (2013) Differential cell line susceptibility to the emerging novel human betacoronavirus 2c EMC/2012: implications for disease pathogenesis and clinical manifestation. *J Infect Dis* 207: 1743-1752

Collier DA, De Marco A, Ferreira I, Meng B, Datir RP, Walls AC, Kemp SA, Bassi J, Pinto D, Silacci-Fregni C *et al* (2021) Sensitivity of SARS-CoV-2 B.1.1.7 to mRNA vaccine-elicited antibodies. *Nature* 593: 136-141

Davies NG, Abbott S, Barnard RC, Jarvis CI, Kucharski AJ, Munday JD, Pearson CAB, Russell TW, Tully DC, Washburne AD *et al* (2021) Estimated transmissibility and impact of SARS-CoV-2 lineage B.1.1.7 in England. *Science* 372

Dimitrov DS (2004) Virus entry: molecular mechanisms and biomedical applications. *Nat Rev Microbiol* 2: 109-122

Dominguez SR, Travanty EA, Qian Z, Mason RJ (2013) Human coronavirus HKU1 infection of primary human type II alveolar epithelial cells: cytopathic effects and innate immune response. *PLoS One* 8: e70129

Edie S, Zaghloul NA, Leitch CC, Klinedinst DK, Lebron J, Thole JF, McCallion AS, Katsanis N, Reeves RH (2018) Survey of Human Chromosome 21 Gene Expression Effects on Early Development in Danio rerio. *G3 (Bethesda)* 8: 2215-2223

Ferreira I, Datir R, Papa G, Kemp S, Meng B, Rakshit P, Singh S, Pandey R, Ponnusamy K, Radhakrishnan VS *et al* (2021) SARS-CoV-2 B.1.617 emergence and sensitivity to vaccine-elicited antibodies. *bioRxiv*: 2021.2005.2008.443253

Frampton D, Rampling T, Cross A, Bailey H, Heaney J, Byott M, Scott R, Sconza R, Price J, Margaritis M *et al* (2021) Genomic characteristics and clinical effect of the emergent SARS-CoV-

2 B.1.1.7 lineage in London, UK: a whole-genome sequencing and hospital-based cohort study. *Lancet Infect Dis*

Franks TJ, Chong PY, Chui P, Galvin JR, Lourens RM, Reid AH, Selbs E, McEvoy CP, Hayden CD, Fukuoka J *et al* (2003) Lung pathology of severe acute respiratory syndrome (SARS): a study of 8 autopsy cases from Singapore. *Hum Pathol* 34: 743-748

Hadjadj J, Yatim N, Barnabei L, Corneau A, Boussier J, Smith N, Pere H, Charbit B, Bondet V, Chenevier-Gobeaux C *et al* (2020) Impaired type I interferon activity and inflammatory responses in severe COVID-19 patients. *Science* 369: 718-724

Hoffmann M, Arora P, Gross R, Seidel A, Hornich BF, Hahn AS, Kruger N, Graichen L, Hofmann-Winkler H, Kempf A *et al* (2021) SARS-CoV-2 variants B.1.351 and P.1 escape from neutralizing antibodies. *Cell* 184: 2384-2393 e2312

Hoffmann M, Kleine-Weber H, Pohlmann S (2020a) A Multibasic Cleavage Site in the Spike Protein of SARS-CoV-2 Is Essential for Infection of Human Lung Cells. *Mol Cell* 78: 779-784 e775

Hoffmann M, Kleine-Weber H, Schroeder S, Kruger N, Herrler T, Erichsen S, Schiergens TS, Herrler G, Wu NH, Nitsche A *et al* (2020b) SARS-CoV-2 Cell Entry Depends on ACE2 and TMPRSS2 and Is Blocked by a Clinically Proven Protease Inhibitor. *Cell* 181: 271-280 e278

Hou YJ, Chiba S, Halfmann P, Ehre C, Kuroda M, Dinnon KH, 3rd, Leist SR, Schafer A, Nakajima N, Takahashi K *et al* (2020) SARS-CoV-2 D614G variant exhibits efficient replication ex vivo and transmission in vivo. *Science* 370: 1464-1468

Huang C, Wang Y, Li X, Ren L, Zhao J, Hu Y, Zhang L, Fan G, Xu J, Gu X *et al* (2020) Clinical features of patients infected with 2019 novel coronavirus in Wuhan, China. *Lancet* 395: 497-506

Jackson L, Rodel H, Hwa S-H, Cele S, Ganga Y, Tegally H, Bernstein M, Giandhari J, Gosnell BI, Khan K *et al* (2021) SARS-CoV-2 cell-to-cell spread occurs rapidly and is insensitive to antibody neutralization. *bioRxiv*: 2021.2006.2001.446516

Jiang X, Zhang Z, Wang C, Ren H, Gao L, Peng H, Niu Z, Ren H, Huang H, Sun Q (2020) Bimodular effects of D614G mutation on the spike glycoprotein of SARS-CoV-2 enhance protein processing, membrane fusion, and viral infectivity. *Signal Transduct Target Ther* 5: 268

Kemp SA, Meng B, Ferriera IA, Datir R, Harvey WT, Papa G, Lytras S, Collier DA, Mohamed A, Gallo G *et al* (2021) Recurrent emergence and transmission of a SARS-CoV-2 spike deletion H69/V70. *bioRxiv*: 2020.2012.2014.422555

Kodaka M, Yang Z, Nakagawa K, Maruyama J, Xu X, Sarkar A, Ichimura A, Nasu Y, Ozawa T, Iwasa H *et al* (2015) A new cell-based assay to evaluate myogenesis in mouse myoblast C2C12 cells. *Exp Cell Res* 336: 171-181

Korber B, Fischer WM, Gnanakaran S, Yoon H, Theiler J, Abfalterer W, Hengartner N, Giorgi EE, Bhattacharya T, Foley B *et al* (2020) Tracking Changes in SARS-CoV-2 Spike: Evidence that D614G Increases Infectivity of the COVID-19 Virus. *Cell* 182: 812-827 e819

Leung K, Shum MH, Leung GM, Lam TT, Wu JT (2021) Early transmissibility assessment of the N501Y mutant strains of SARS-CoV-2 in the United Kingdom, October to November 2020. *Euro Surveill* 26

Li W, Moore MJ, Vasilieva N, Sui J, Wong SK, Berne MA, Somasundaran M, Sullivan JL, Luzuriaga K, Greenough TC *et al* (2003) Angiotensin-converting enzyme 2 is a functional receptor for the SARS coronavirus. *Nature* 426: 450-454

Liu Y, Liu J, Plante KS, Plante JA, Xie X, Zhang X, Ku Z, An Z, Scharton D, Schindewolf C *et al* (2021a) The N501Y spike substitution enhances SARS-CoV-2 transmission. *bioRxiv*: 2021.2003.2008.434499

Liu Y, Liu J, Plante KS, Plante JA, Xie X, Zhang X, Ku Z, An Z, Scharton D, Schindewolf C *et al* (2021b) The N501Y spike substitution enhances SARS-CoV-2 transmission. *bioRxiv*

Liu Z, VanBlargan LA, Bloyet LM, Rothlauf PW, Chen RE, Stumpf S, Zhao H, Errico JM, Theel ES, Liebeskind MJ *et al* (2021c) Identification of SARS-CoV-2 spike mutations that attenuate monoclonal and serum antibody neutralization. *Cell Host Microbe* 29: 477-488 e474

Luan B, Wang H, Huynh T (2021) Molecular Mechanism of the N501Y Mutation for Enhanced Binding between SARS-CoV-2's Spike Protein and Human ACE2 Receptor. *bioRxiv*: 2021.2001.2004.425316

Nelson G, Buzko O, Spilman P, Niazi K, Rabizadeh S, Soon-Shiong P (2021) Molecular dynamic simulation reveals E484K mutation enhances spike RBD-ACE2 affinity and the combination of

E484K, K417N and N501Y mutations (501Y.V2 variant) induces conformational change greater than N501Y mutant alone, potentially resulting in an escape mutant. *bioRxiv*: 2021.2001.2013.426558

Pizzorno A, Padey B, Julien T, Trouillet-Assant S, Traversier A, Errazuriz-Cerda E, Fouret J, Dubois J, Gaymard A, Lescure FX *et al* (2020) Characterization and Treatment of SARS-CoV-2 in Nasal and Bronchial Human Airway Epithelia. *Cell Rep Med* 1: 100059

Planas D, Bruel T, Grzelak L, Guivel-Benhassine F, Staropoli I, Porrot F, Planchais C, Buchrieser J, Rajah MM, Bishop E *et al* (2021a) Sensitivity of infectious SARS-CoV-2 B.1.1.7 and B.1.351 variants to neutralizing antibodies. *Nat Med*

Planas D, Veyer D, Baidaliuk A, Staropoli I, Guivel-Benhassine F, Rajah MM, Planchais C, Porrot F, Robillard N, Puech J *et al* (2021b) Reduced sensitivity of infectious SARS-CoV-2 variant B.1.617.2 to monoclonal antibodies and sera from convalescent and vaccinated individuals. *bioRxiv*: 2021.2005.2026.445838

Qian Z, Dominguez SR, Holmes KV (2013) Role of the spike glycoprotein of human Middle East respiratory syndrome coronavirus (MERS-CoV) in virus entry and syncytia formation. *PLoS One* 8: e76469

Ramanathan M, Ferguson ID, Miao W, Khavari PA (2021) SARS-CoV-2 B.1.1.7 and B.1.351 spike variants bind human ACE2 with increased affinity. *Lancet Infect Dis*

745 Rees-Spear C, Muir L, Griffith SA, Heaney J, Aldon Y, Snitselaar JL, Thomas P, Graham C, Seow J,
746 Lee N *et al* (2021) The effect of spike mutations on SARS-CoV-2 neutralization. *Cell Rep* 34:
747 108890

748 Robinot R, Hubert M, de Melo GD, Lazarini F, Bruel T, Smith N, Levallois S, Larrous F, Fernandes
749 J, Gellenoncourt S *et al* (2020) SARS-CoV-2 infection damages airway motile cilia and impairs
750 mucociliary clearance. *bioRxiv*: 2020.2010.2006.328369

751 Sabino EC, Buss LF, Carvalho MPS, Prete CA, Jr., Crispim MAE, Fraiji NA, Pereira RHM, Parag KV,
752 da Silva Peixoto P, Kraemer MUG *et al* (2021) Resurgence of COVID-19 in Manaus, Brazil,
753 despite high seroprevalence. *Lancet* 397: 452-455

754 Sanders DW, Jumper CC, Ackerman PJ, Bracha D, Donlic A, Kim H, Kenney D, Castello-Serrano I,
755 Suzuki S, Tamura T *et al* (2021) SARS-CoV-2 requires cholesterol for viral entry and pathological
756 syncytia formation. *Elife* 10

757 Shi G, Kenney AD, Kudryashova E, Zani A, Zhang L, Lai KK, Hall-Stoodley L, Robinson RT,
758 Kudryashov DS, Compton AA *et al* (2021) Opposing activities of IFITM proteins in SARS-CoV-2
759 infection. *EMBO J* 40: e106501

760 Starr TN, Greaney AJ, Addetia A, Hannon WW, Choudhary MC, Dingens AS, Li JZ, Bloom JD
761 (2021) Prospective mapping of viral mutations that escape antibodies used to treat COVID-19.
762 *Science* 371: 850-854

Tegally H, Wilkinson E, Giovanetti M, Iranzadeh A, Fonseca V, Giandhari J, Doolabh D, Pillay S, San EJ, Msomi N *et al* (2020) Emergence and rapid spread of a new severe acute respiratory syndrome-related coronavirus 2 (SARS-CoV-2) lineage with multiple spike mutations in South Africa. *medRxiv*: 2020.2012.2021.20248640

Thorne LG, Bouhaddou M, Reuschl A-K, Zuliani-Alvarez L, Polacco B, Pelin A, Batra J, Whelan MVX, Ummadi M, Rojc A *et al* (2021) Evolution of enhanced innate immune evasion by the SARS-CoV-2 B.1.1.7 UK variant. *bioRxiv*: 2021.2006.2006.446826

Tian F, Tong B, Sun L, Shi S, Zheng B, Wang Z, Dong X, Zheng P (2021) Mutation N501Y in RBD of Spike Protein Strengthens the Interaction between COVID-19 and its Receptor ACE2. *bioRxiv*: 2021.2002.2014.431117

Tian S, Hu W, Niu L, Liu H, Xu H, Xiao SY (2020) Pulmonary Pathology of Early-Phase 2019 Novel Coronavirus (COVID-19) Pneumonia in Two Patients With Lung Cancer. *J Thorac Oncol* 15: 700-704

Touret F, Luciani L, Baronti C, Cochin M, Driouich J-S, Gilles M, Thirion L, Nougairède A, de Lamballerie X (2021) Replicative fitness SARS-CoV-2 20I/501Y.V1 variant in a human reconstituted bronchial epithelium. *bioRxiv*: 2021.2003.2022.436427

van der Made CI, Simons A, Schuurs-Hoeijmakers J, van den Heuvel G, Mantere T, Kersten S, van Deuren RC, Steehouwer M, van Reijmersdal SV, Jaeger M *et al* (2020) Presence of Genetic Variants Among Young Men With Severe COVID-19. *JAMA* 324: 663-673

Weisblum Y, Schmidt F, Zhang F, DaSilva J, Poston D, Lorenzi JCC, Muecksch F, Rutkowska M, Hoffmann HH, Michailidis E *et al* (2020) Escape from neutralizing antibodies by SARS-CoV-2 spike protein variants. *bioRxiv*

Xu Z, Shi L, Wang Y, Zhang J, Huang L, Zhang C, Liu S, Zhao P, Liu H, Zhu L *et al* (2020) Pathological findings of COVID-19 associated with acute respiratory distress syndrome. *Lancet Respir Med* 8: 420-422

Yadav PD, Sapkal GN, Abraham P, Ella R, Deshpande G, Patil DY, Nyayanit DA, Gupta N, Sahay RR, Shete AM *et al* (2021) Neutralization of variant under investigation B.1.617 with sera of BBV152 vaccinees. *bioRxiv*: 2021.2004.2023.441101

Yurkovetskiy L, Wang X, Pascal KE, Tomkins-Tinch C, Nyalile TP, Wang Y, Baum A, Diehl WE, Dauphin A, Carbone C *et al* (2020) Structural and Functional Analysis of the D614G SARS-CoV-2 Spike Protein Variant. *Cell* 183: 739-751 e738

Zahradník J, Marciano S, Shemesh M, Zoler E, Chiaravalli J, Meyer B, Rudich Y, Dym O, Elad N, Schreiber G (2021) SARS-CoV-2 RBD in vitro evolution follows contagious mutation spread, yet generates an able infection inhibitor. *bioRxiv*: 2021.2001.2006.425392

Zhang X, Tan Y, Ling Y, Lu G, Liu F, Yi Z, Jia X, Wu M, Shi B, Xu S *et al* (2020) Viral and host factors related to the clinical outcome of COVID-19. *Nature* 583: 437-440

Zhang Z, Zheng Y, Niu Z, Zhang B, Wang C, Yao X, Peng H, Franca DN, Wang Y, Zhu Y *et al* (2021) SARS-CoV-2 spike protein dictates syncytium-mediated lymphocyte elimination. *Cell Death Differ*

Zhou Z, Ren L, Zhang L, Zhong J, Xiao Y, Jia Z, Guo L, Yang J, Wang C, Jiang S *et al* (2020) Heightened Innate Immune Responses in the Respiratory Tract of COVID-19 Patients. *Cell Host Microbe* 27: 883-890 e882

Zhu N, Wang W, Liu Z, Liang C, Wang W, Ye F, Huang B, Zhao L, Wang H, Zhou W *et al* (2020) Morphogenesis and cytopathic effect of SARS-CoV-2 infection in human airway epithelial cells. *Nat Commun* 11: 3910

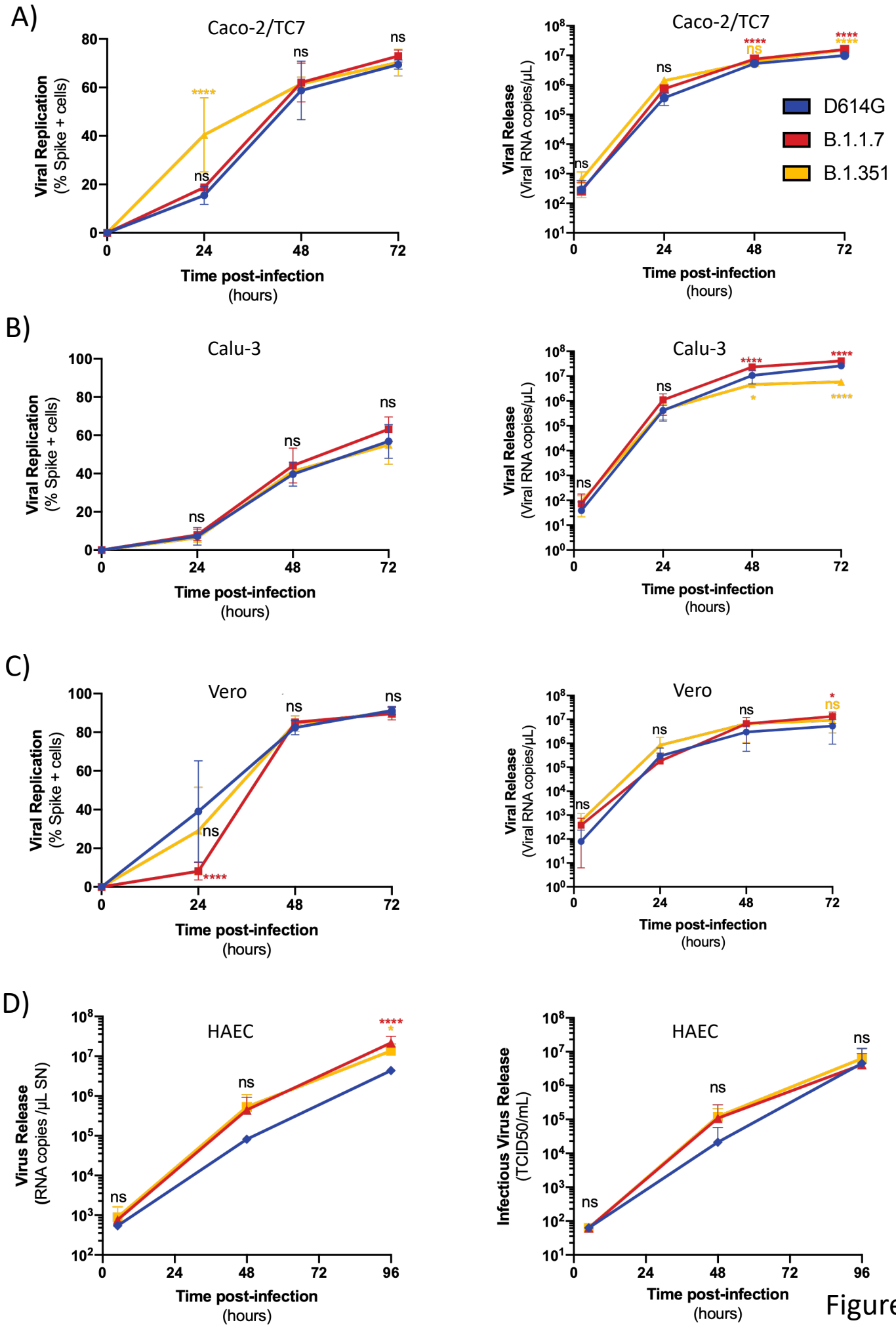
A)
Caco-2/TC7
Viral Replication
(% Spike + cells)
Time post-infection
(hours)
Caco-2/TC7
Viral Release
(Viral RNA copies/µL)
Time post-infection
(hours)
D614G
B.1.1.7
B.1.351
B)
Calu-3
Viral Replication
(% Spike + cells)
Time post-infection
(hours)
Calu-3
Viral Release
(Viral RNA copies/µL)
Time post-infection
(hours)
C)
Vero
Viral Replication
(% Spike + cells)
Time post-infection
(hours)
Vero
Viral Release
(Viral RNA copies/µL)
Time post-infection
(hours)
D)
HAEC
Virus Release
(RNA copies /µL SN)
Time post-infection
(hours)
HAEC
Infectious Virus Release
(TCID50/mL)
Time post-infection
(hours)

Figure 1

A)

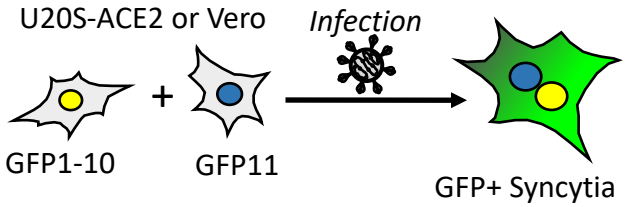
U20S-ACE2 or Vero
Infection
GFP1-10
GFP11
GFP+ Syncytia

B)

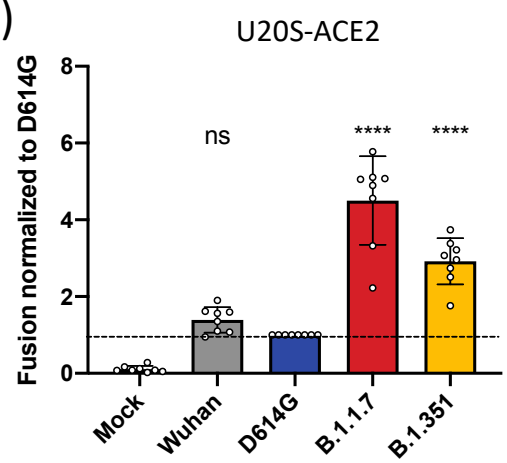
U20S-ACE2
Fusion normalized to D614G
8
6
4
2
0
ns
****
****
Mock
Wuhan
D614G
B.1.1.7
B.1.351

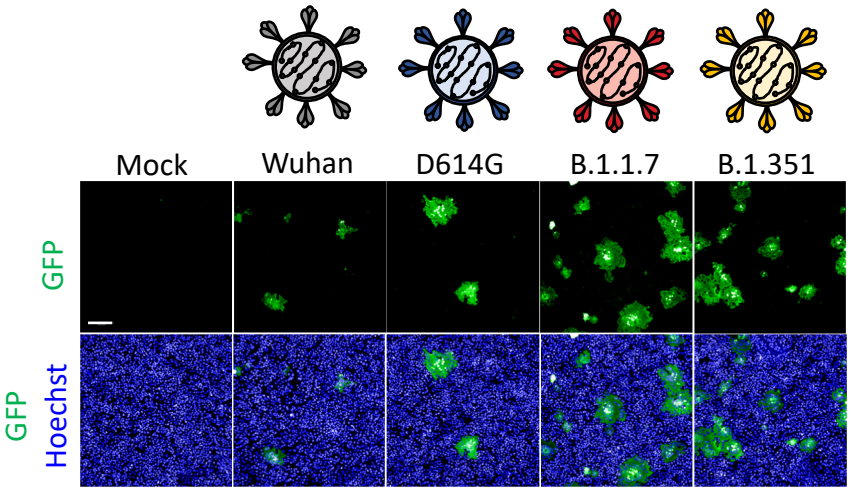
Mock
Wuhan
D614G
B.1.1.7
B.1.351
GFP
GFP
Hoechst

C)

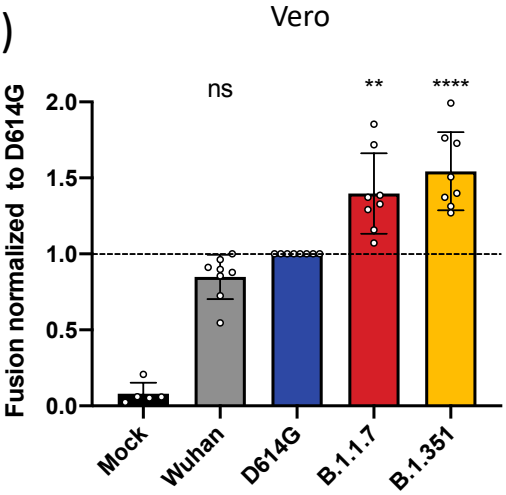
Vero
Fusion normalized to D614G
2.0
1.5
1.0
0.5
0.0
ns
**
****
Mock
Wuhan
D614G
B.1.1.7
B.1.351

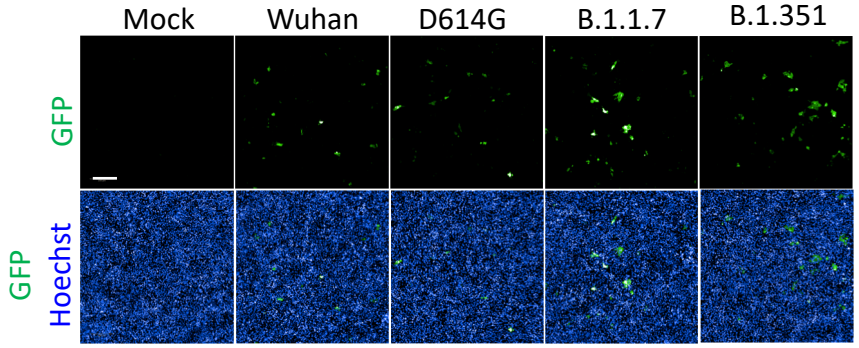
Mock
Wuhan
D614G
B.1.1.7
B.1.351
GFP
GFP
Hoechst

Figure 2

A)

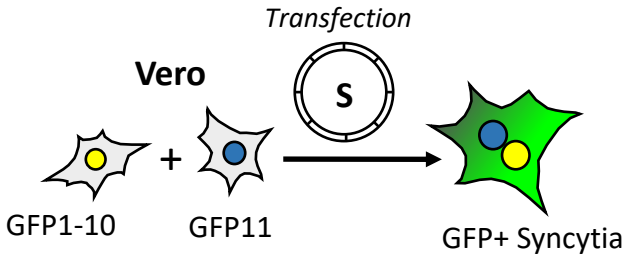
Transfection
Vero
S
GFP1-10
GFP11
GFP+ Syncytia

B)

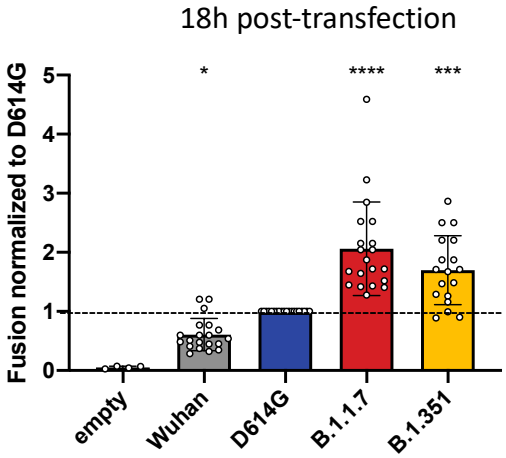
18h post-transfection
Fusion normalized to D614G
5
4
3
2
1
0
*
****
***
empty
Wuhan
D614G
B.1.1.7
B.1.351

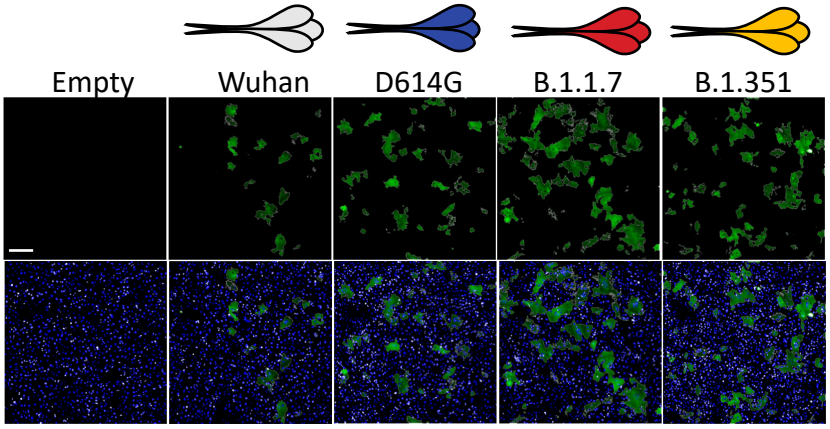
Empty
Wuhan
D614G
B.1.1.7
B.1.351

C)

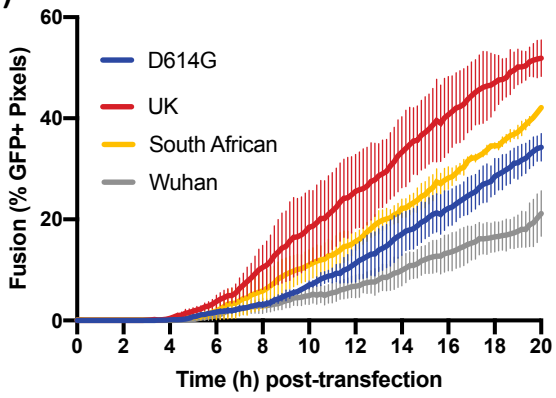
Fusion (% GFP+ Pixels)
60
40
20
0
D614G
UK
South African
Wuhan
0
2
4
6
8
10
12
14
16
18
20
Time (h) post-transfection

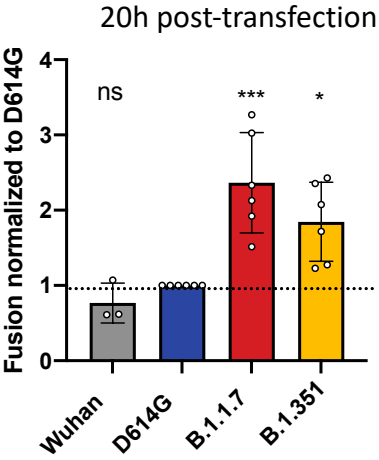
20h post-transfection
Fusion normalized to D614G
4
3
2
1
0
ns
***
*
Wuhan
D614G
B.1.1.7
B.1.351

Figure 3

A)

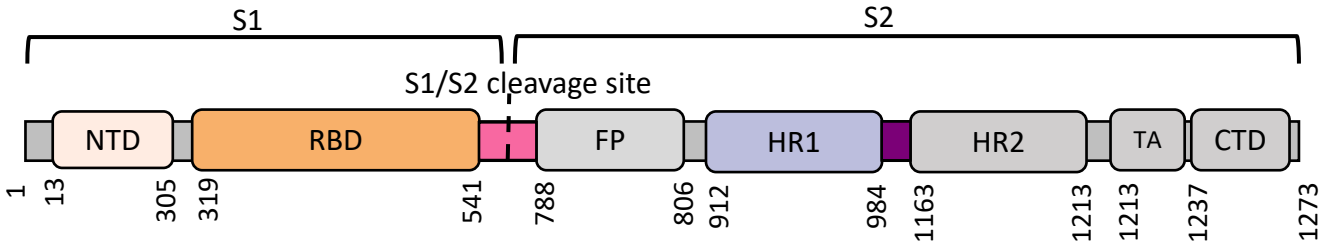
S1
S2
S1/S2 cleavage site
NTD
RBD
FP
HR1
HR2
TA
CTD
1
13
305
319
541
788
806
912
984
1163
1213
1213
1237
1273

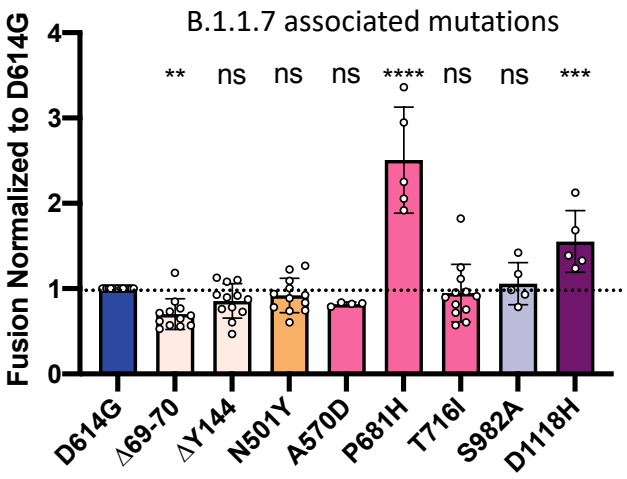
B.1.1.7 associated mutations
Fusion Normalized to D614G
0
1
2
3
4
** ns ns ns **** ns ns ***
D614G
Δ69-70
ΔY144
N501Y
A570D
P681H
T716I
S982A
D1118H

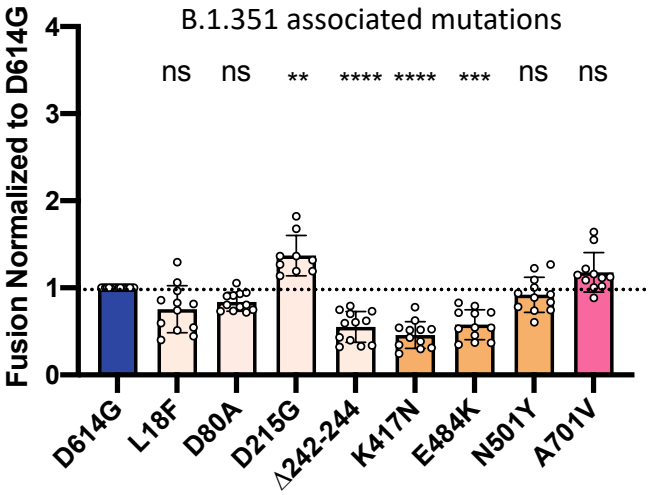
B.1.351 associated mutations
Fusion Normalized to D614G
0
1
2
3
4
ns ns ** **** **** *** ns ns
D614G
L18F
D80A
D215G
Δ242-244
K417N
E484K
N501Y
A701V

B)

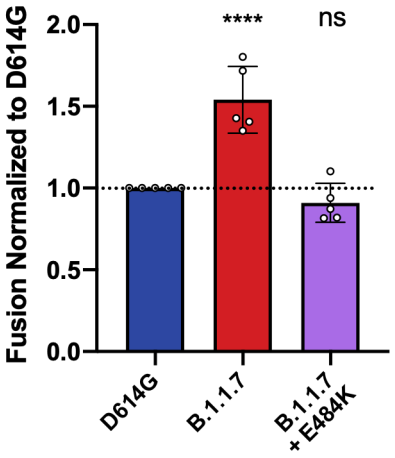
Fusion Normalized to D614G
0.0
0.5
1.0
1.5
2.0
**** ns
D614G
B.1.1.7
B.1.1.7 + E484K

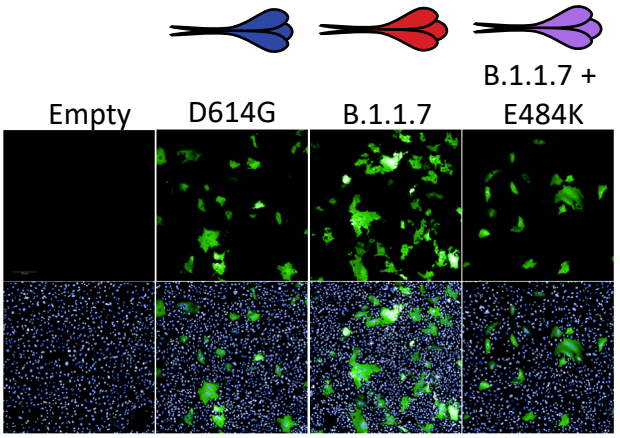
Empty
D614G
B.1.1.7
B.1.1.7 + E484K

Figure 4

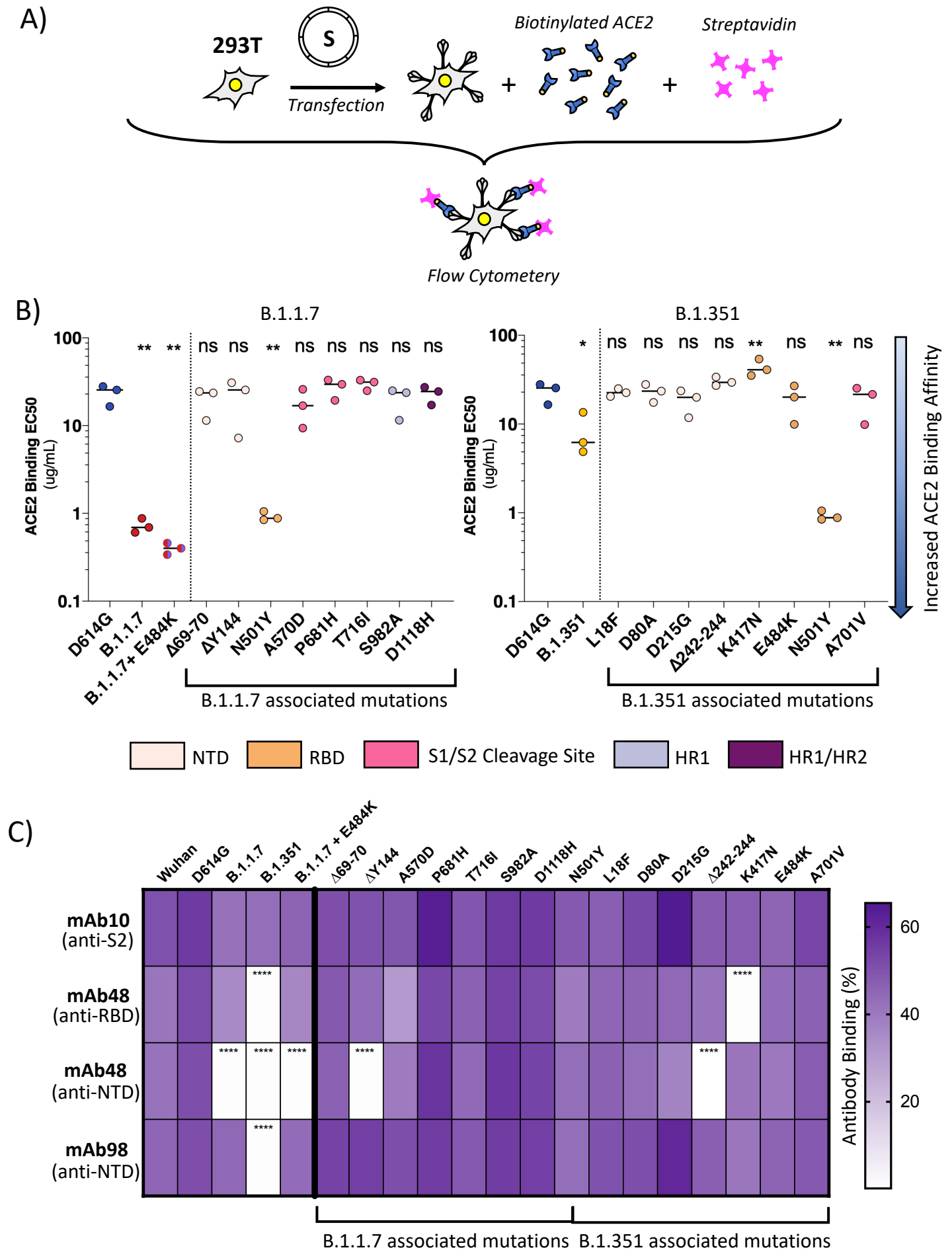
A)
293T
S
Transfection
Biotinylated ACE2
Streptavidin
Flow Cytometery
B)
B.1.1.7
B.1.351
ACE2 Binding EC50 (ug/mL)
100
10
1
0.1
** **
ns ns ** ns ns ns ns ns
* ns ns ns ns ** ns ** ns
D614G
B.1.1.7
B.1.1.7+ E484K
Δ69-70
ΔY144
N501Y
A570D
P681H
T716I
S982A
D1118H
B.1.351
L18F
D80A
D215G
Δ242-244
K417N
E484K
A701V
B.1.1.7 associated mutations
B.1.351 associated mutations
Increased ACE2 Binding Affinity
NTD
RBD
S1/S2 Cleavage Site
HR1
HR1/HR2
C)
Wuhan
D614G
B.1.1.7
B.1.351
B.1.1.7 + E484K
Δ69-70
ΔY144
A570D
P681H
T716I
S982A
D1118H
N501Y
L18F
D80A
D215G
Δ242-244
K417N
E484K
A701V
mAb10 (anti-S2)
mAb48 (anti-RBD)
mAb48 (anti-NTD)
mAb98 (anti-NTD)
****
Antibody Binding (%)
60
40
20
B.1.1.7 associated mutations
B.1.351 associated mutations

Figure 5

Expanded View Figures

A)

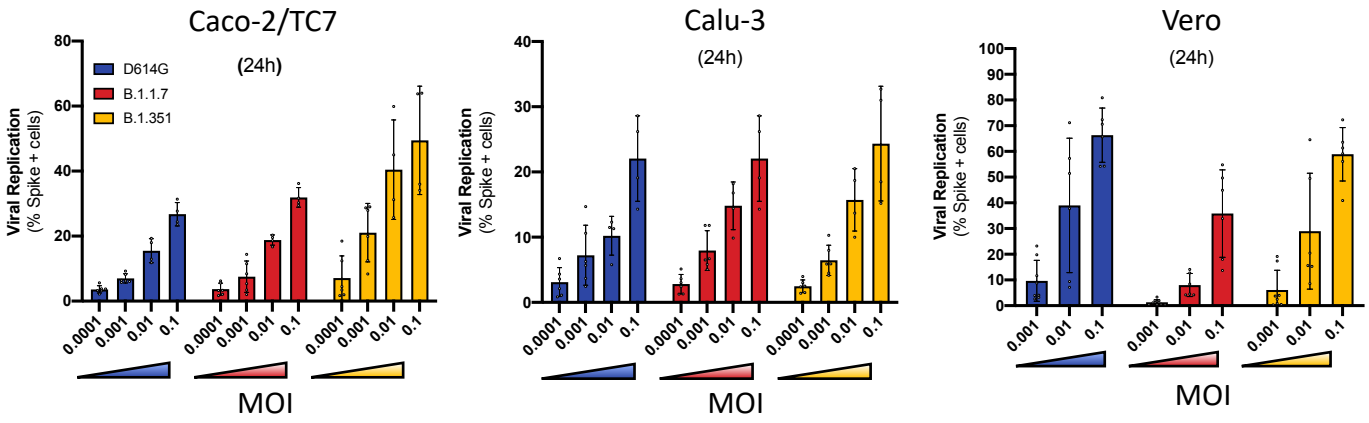

B)

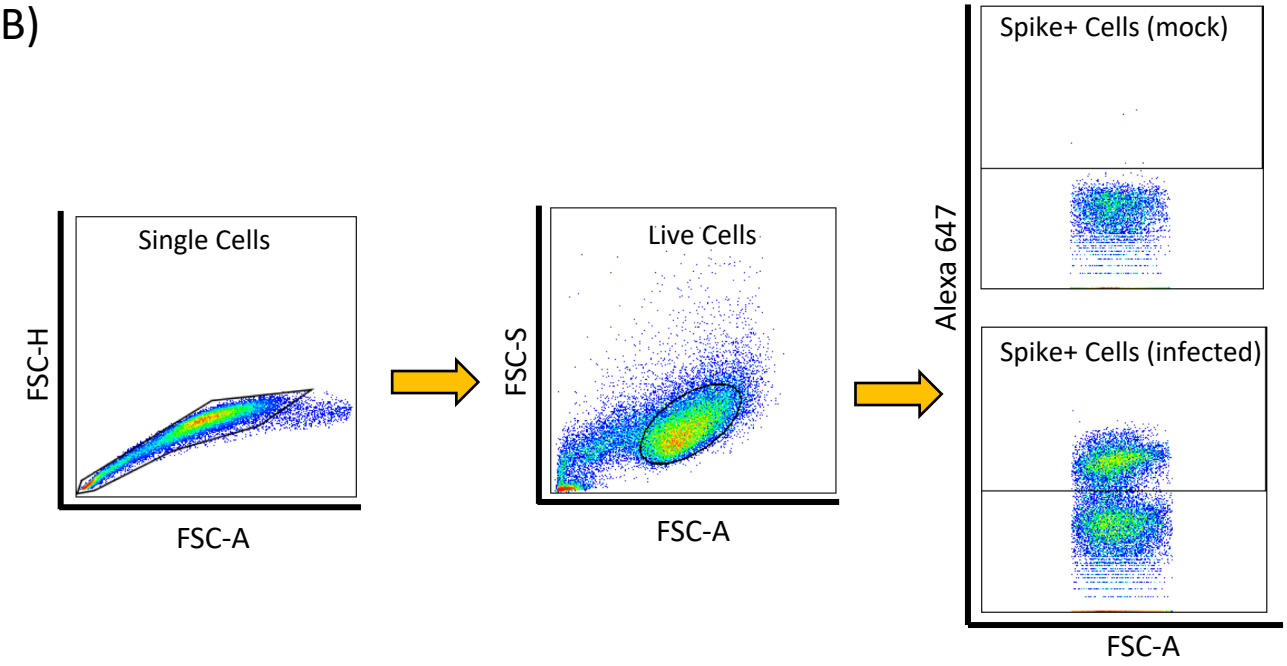

C)

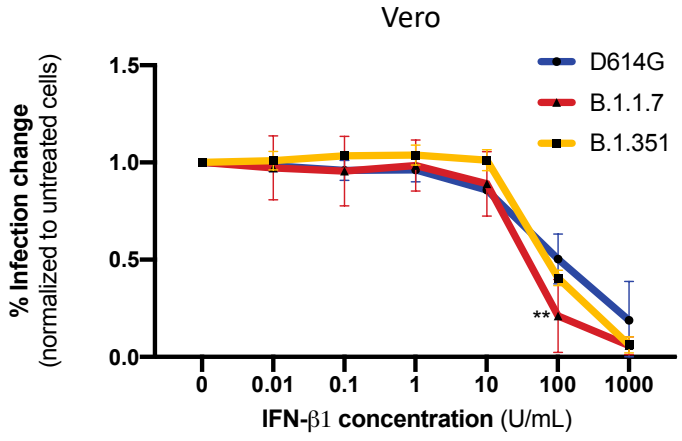

Expanded View 1

A)

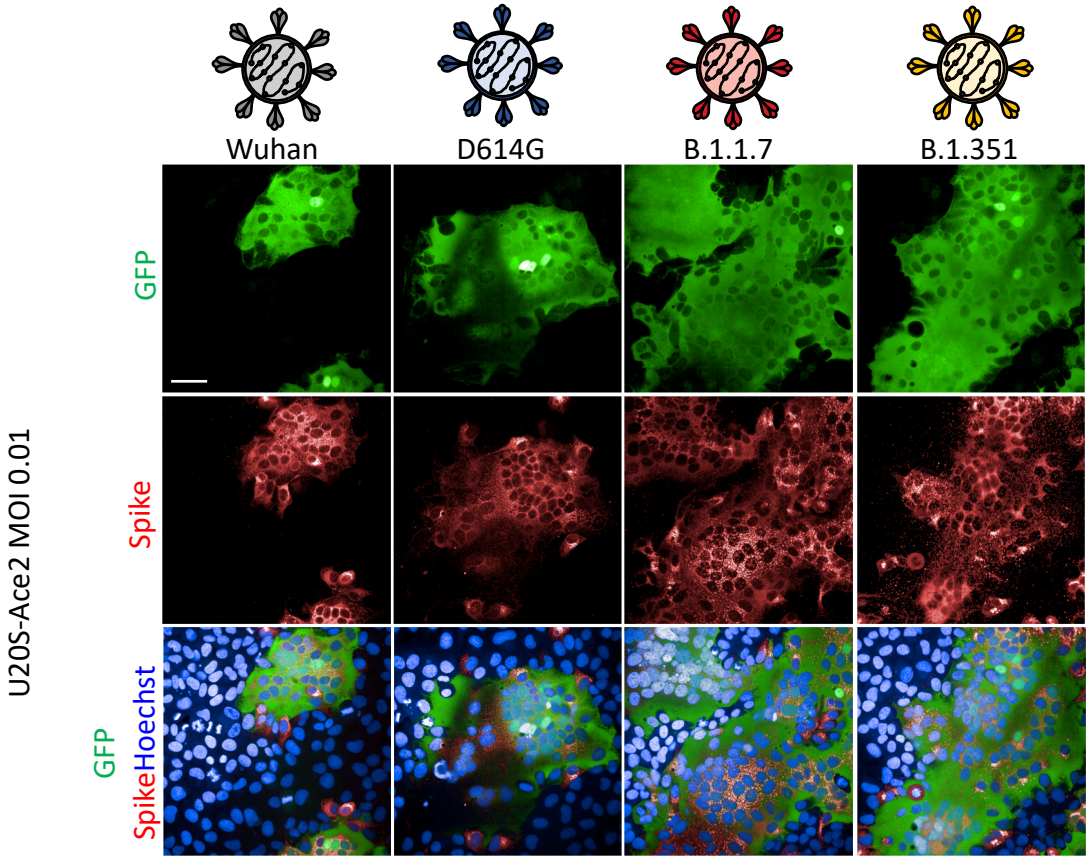

B)

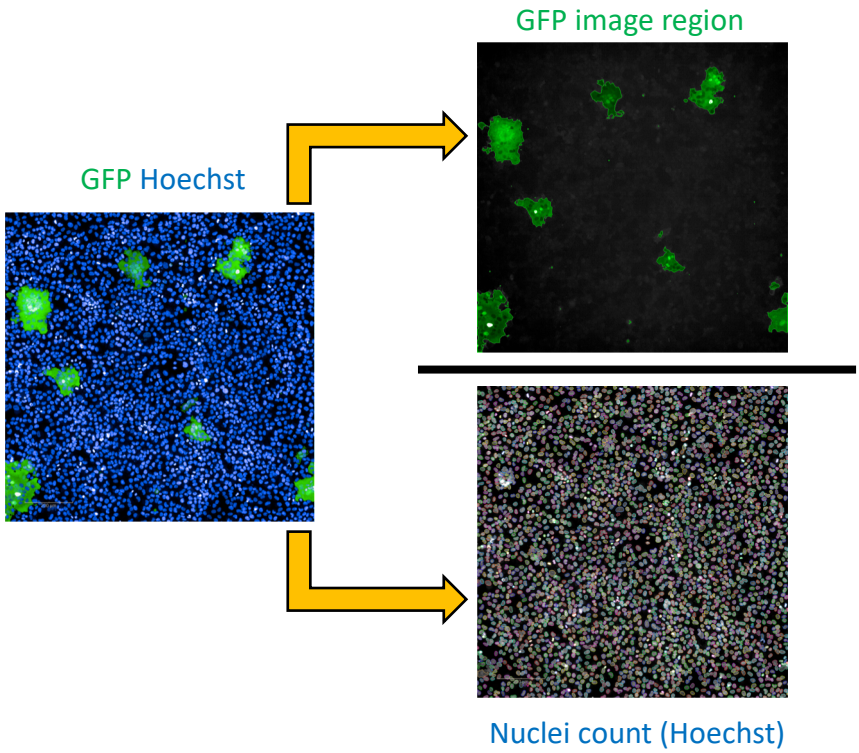

Expanded View 2

A)

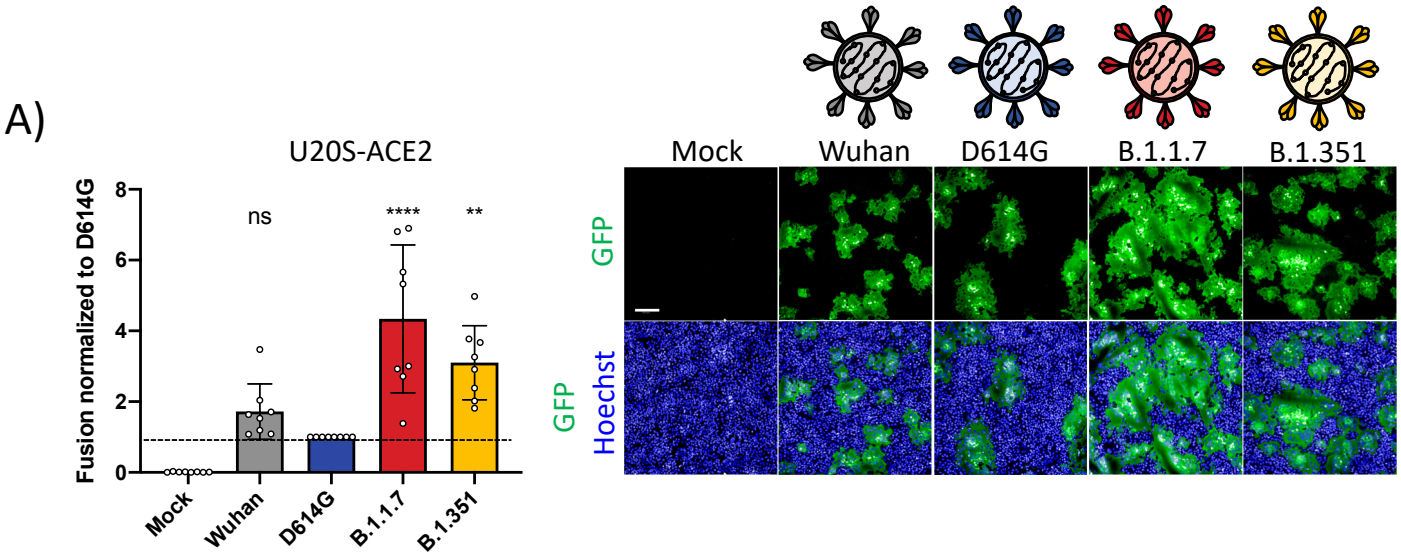

B)

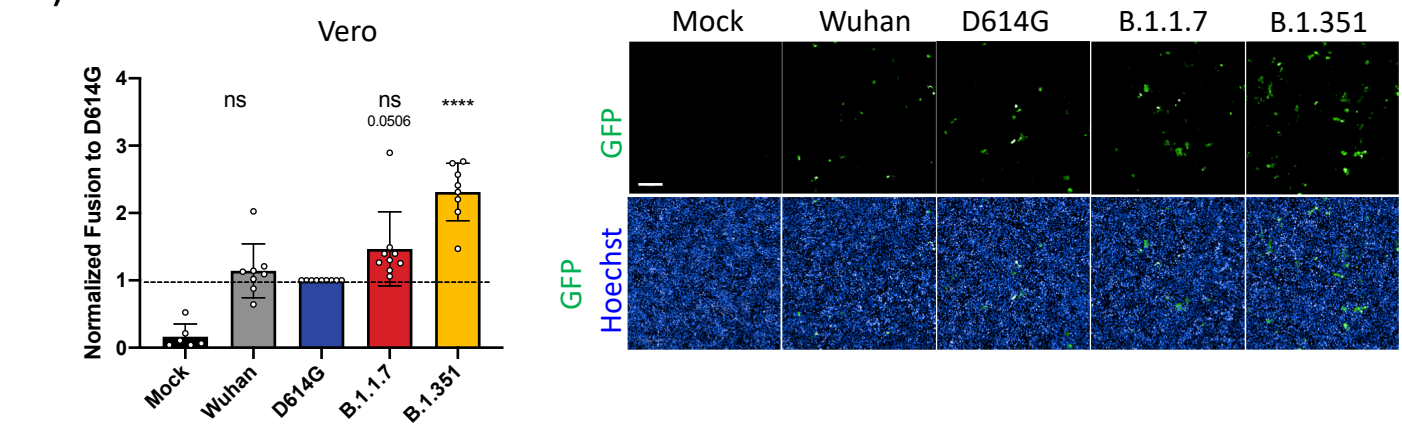

C)

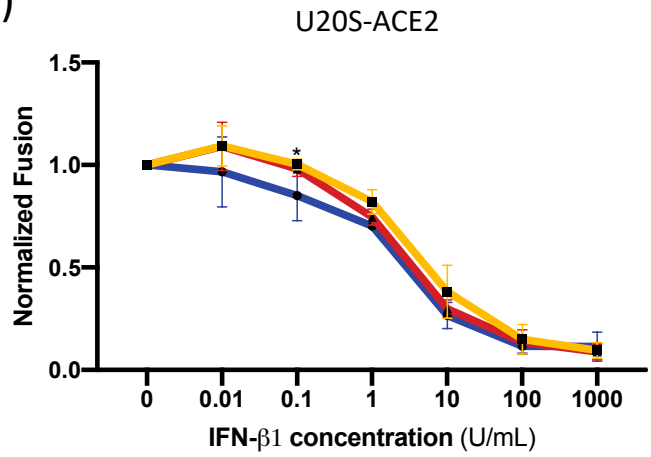

Expanded View 3

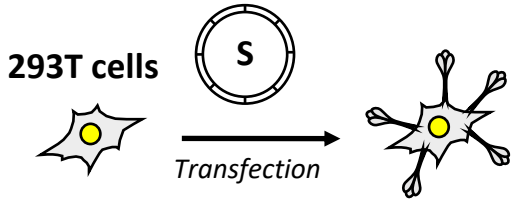

A)

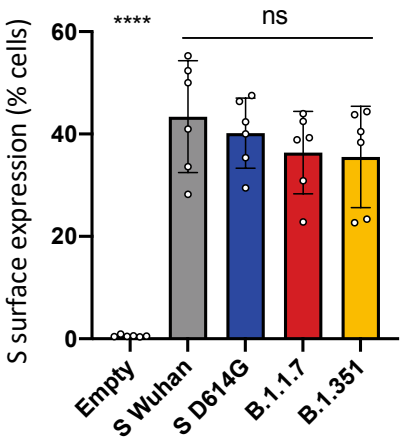

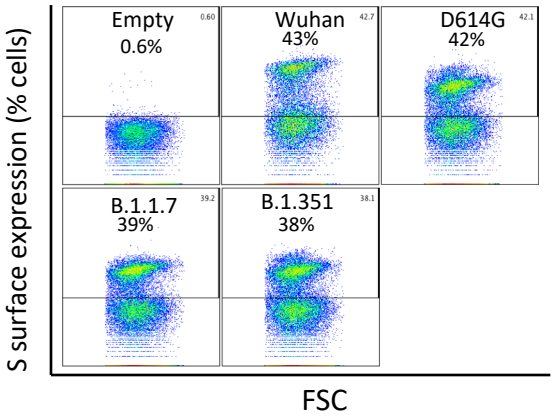

B)

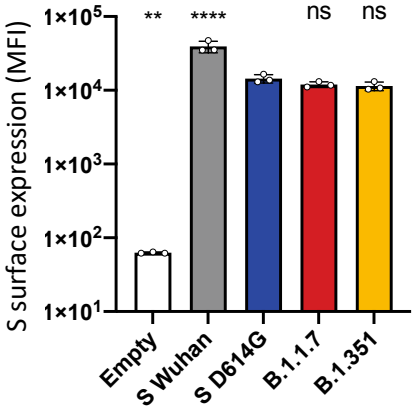

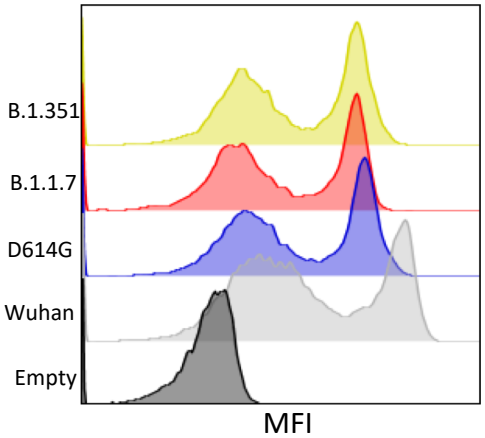

C)

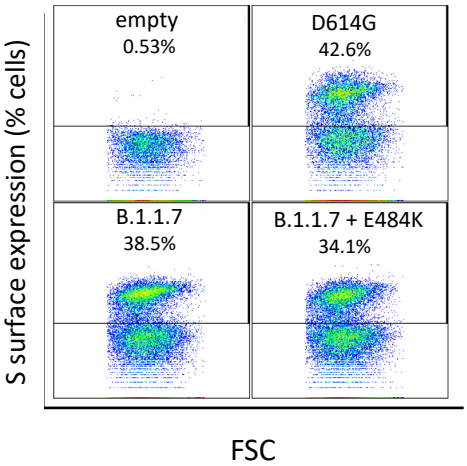

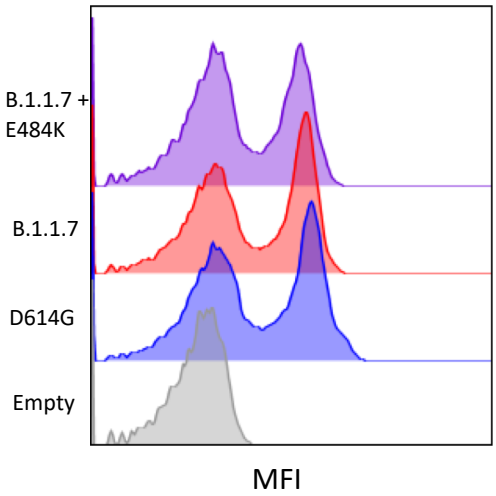

Expanded View 4

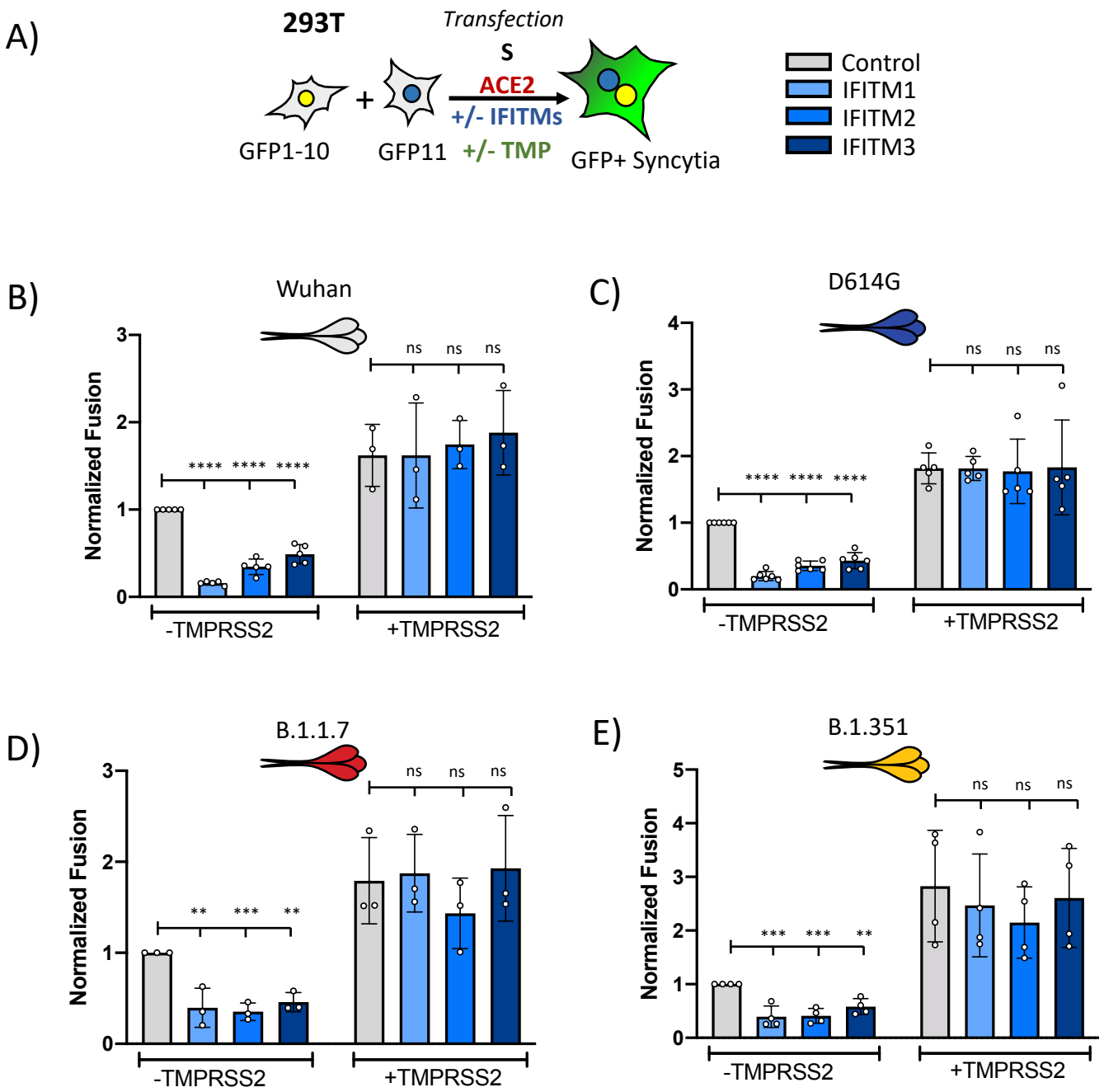

Expanded View 5

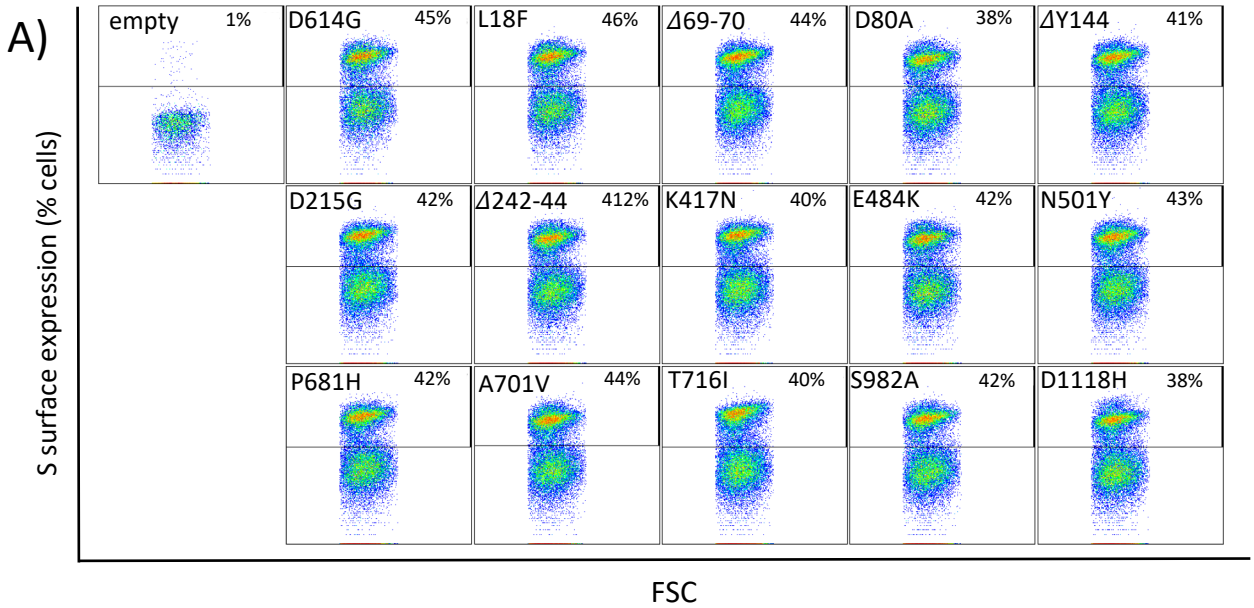

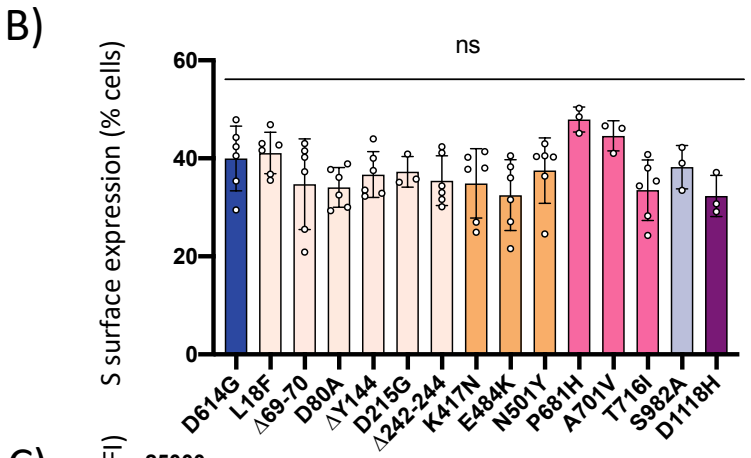

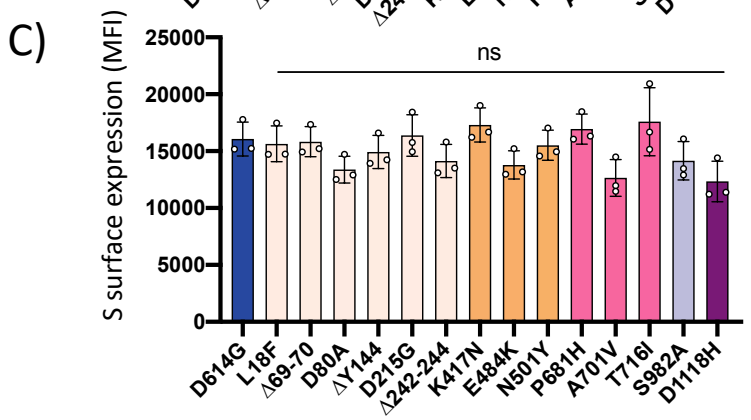

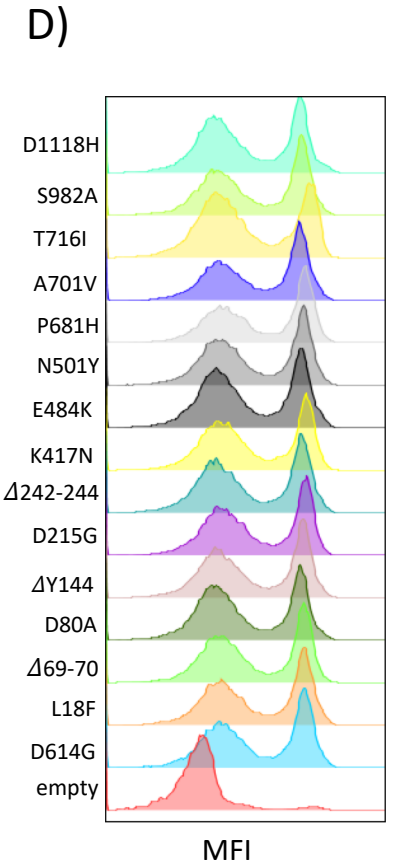

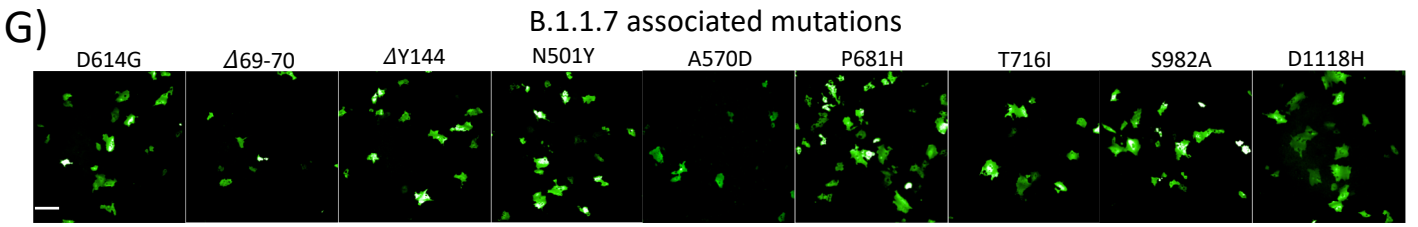

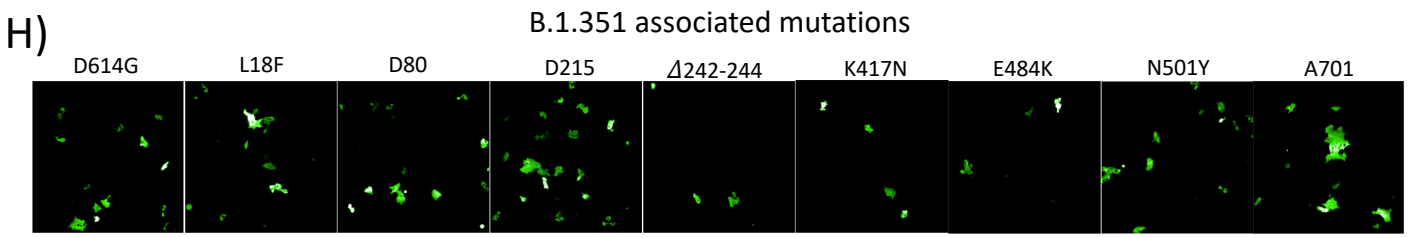

Expanded View 6

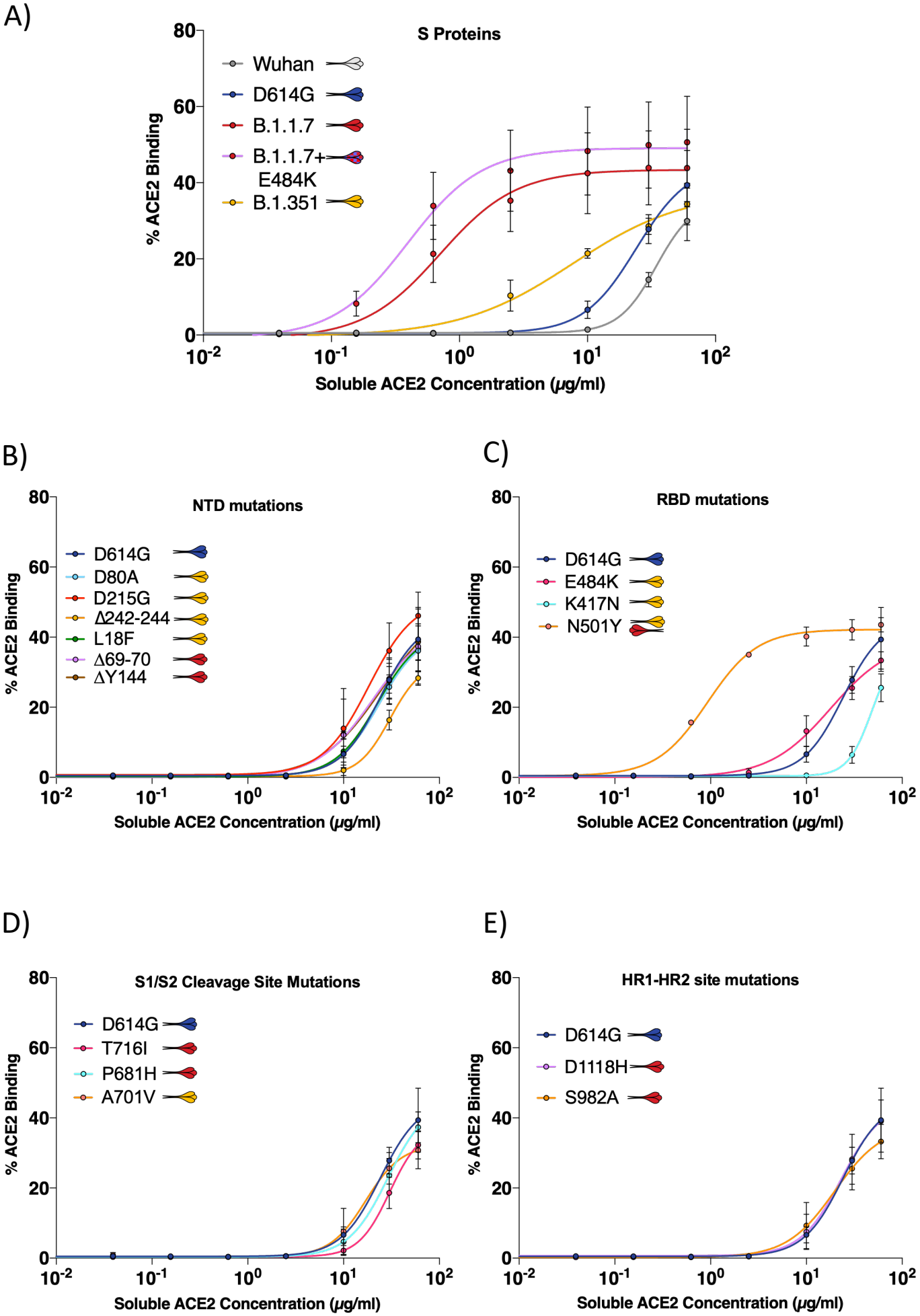

Expanded View 7

Table 1: Sequecing and qRT-PCR primers

Primer name	Sequence (5'-3')
Sequencing Primers	
phCMV For	CTCTTTCCTACAGCTCCTGG
phCMV Rev	TAGCCAGAAGTCAGATGCTC
phCMV Int1 For	AGCGAGTTCCGCGTGTACAG
phCMV Int2 For	CGCAAGCGCATTAGCAACTG
phCMV Int3 For	GCGTGCTGACCGAGAGTAAC
phCMV Int4 For	GCAACCTGCTGCTGCAGTAC
phCMV Int5 For	GTGGTCAACCAGAACGCTCAG
phCMV Int6 For	AGAACCACACAAGCCCCGAC
qRT-PCR Primers	**SARS-CoV-2 N protein specific**
For	TAATCAGAC15AAGGAACTGATTA
Rev	CGAAGGTGTGACTTCCATG

Table 2: Site directed mutagenesis primers

Mutant	Site Directed Mutagenesis Primers (5'-3')
D614G	For : CTGTACCAGGgcGTGAATTGCACAGAGGTG Rev : AACGGCCACCTGGTTGCT
L18F	For : GTGCGTGAACttcACCACACGAAC Rev TGACTGGACACCAGTGGC
Δ69-70	For : TCCGGCACCAATGGCACC Rev : GATGGCGTGGAACCAGGTC
D80A	For : AAGCGCTTCGcTAATCCCGTGC Rev : GGTGCCATTGGTGCCGGA
Y144	For : TACCACAAGAACAACAAGAGCTGG Rev : GACGCCCAGGAAGGGGTC
D215G	For : CTCGTGCGCGgcCTGCCACAGG Rev : GTTGATTGGGGTGTGCTTG
Δ242-244	For : CACCGCAGTTACTTGACAC Rev : CAGTGTCTGAAAGCGGGT
K417N	For : AGACCGGCAAcATCGCCGACTAC Rev : GGCCTGGGGCAATCTGTC
E484K	For : CAACGGCGTGaAAGGCTTCAACTG Rev : CATGGGGTGCTTCCGGCC
N501Y	For : TCAGCCCACAtATGGCGTGGG Rev : AATCCGTAGGACTGCAGTG
A570D	For : CGCGACATTGaCGATACAACC Rev : GCCAAACTGCTGGAATGG
P681H	For : ACCAATAGTCacCGACGAGCCC Rev : CTGGGTCTGATAGGAGGC
A701V	For : AGCCTGGGCGtgGAGAATAGCG Rev : CATGGTATAGGCAATGATG
T716I	For : GCTATCCCCAtCAACTTCACC Rev : AATGCTGTTGTTGGAGTAG
S982A	For : CGATATCCTGgcCCGCCTGGATAAG Rev : TTCAGCACGCTACTGATG
D1118H	For : CATCACCACCcACAACACCTTC Rev : ATCTGGGGCTCGTAGAAG